IRC +10 216 revisited

I. The circumstellar dust shell[*]

M.A.T. Groenewegen

Max-Planck-Institut für Astrophysik, Karl-Schwarzschild-Straße 1, D-85740 Garching, Germany

Abstract. A spherically symmetric dust radiative transfer code is used to model the circumstellar dust shell around IRC +10 216. Compared to numerous previous models a much larger body of observational data is used as constraints; the spectral energy distribution between 0.5 and 60000 μm, 2-4 μm and 8-23 μm spectra, optical, far-infrared and centimeter sizes and interferometric visibility curves between 1.6 and 11.2 μm are used to constrain the model.

The most important result is that in order to fit the visibility curve at 2.2 μm and the size of the shell in the optical, scattering has to be invoked. The strong dependence of the scattering coefficient on grain size allows one to derive a mean grain size of 0.16 $\pm$ 0.01 μm.

For a model with a r^{-2} density distribution a dust mass loss rate of 8.1 $\pm$ 0.7 $\times$ 10^{-7} D (kpc) M$_\odot$ yr^{-1} (adopting v$_\infty$ = 17.5 km s^{-1} and a dust opacity $\kappa_{60\mu m}$ = 68 cm^{2}g^{-1}), a luminosity at maximum light of 823 $\pm$ 40 $\times$ 10^3 $(D$ (kpc))^2 L$_\odot$, an inner dust radius of r_c = 4.5 $\pm$ 0.5 $R_\star$, an inner dust temperature of T_c = 1075 $\pm$ 50 K and an effective temperature of T_{eff} = 2000 $\pm$ 100 K are derived (all 1σ error bars).

It is found that a r^{-2} dust density law in the inner part of the shell gives a slightly better fit than the physically more realistic case of a steeper law where the effect of the increasing dust velocity with radius is taken into account. It is suggested that the dust-to-gas ratio *also* increases with radius and that therefore the net effect on the dust density distribution may be small.

Previous suggestions that the mass loss rate was higher in the past are confirmed. The principle argument is that with an r^{-2} model the calculated far-infrared sizes are smaller than observed. A good fit is obtained with a dust mass loss rate of 8.1 $\times$ 10^{-7} D (kpc) M$_\odot$ yr^{-1} for r < 123$''$ and 7.3 $\times$ 10^{-6} D (kpc) M$_\odot$ yr^{-1} for r > 123$''$ (assuming that v$_\infty$ and the dust opacity do not change with time). An alternative model with an exponentially decreasing mass loss rate can be excluded.

The presently available constraints are not sensitive to the dust density beyond $\sim$10$'$. The total dust mass in the shell out to 10$'$ is 1.0 $(D$ (kpc))^2 M$_\odot$ in the model with the non constant mass loss rate, and 0.13 $(D$ (kpc))^2 M$_\odot$ in the model with the constant mass loss rate.

The slope of the dust opacity beyond $\sim$1000 μm (where no laboratory measurements are available) and the influence of free-free emission are investigated by comparing cm-observations to a newly developed radiative transfer code to calculate the emission from a central star surrounded by a shell where free-free emission is assumed to occur. It is found that in small apertures dust emission is negligible for wavelengths $\gtrsim$ 2 cm. Free-free emission is negligible for wavelengths $\lesssim$0.5 cm. To account for the observed flux at 3300 μm the slope of the opacity is changed to $Q_\lambda \sim \lambda^{-0.85}$ for λ > 1000 μm. The free-free emission is found to be optically thin even at 6 cm. An ionization fraction of 7.8 $\times$ 10^{-5} is derived which, according to the Saha equation, corresponds to an electron temperature of about 2400 K. Although there are uncertainties in the free-free emission model this suggests that the free-free emission does not come from a chromosphere.

Key words: circumstellar matter – stars: individual: IRC +10 216 – stars: mass loss – stars: AGB, post-AGB – infrared: stars

1. Introduction

IRC +10 216 (= AFGL 1381 = CW Leo) is the best studied carbon star in the universe (by humans). One aspect of study has traditionally been the properties of the circumstellar dust shell: what is the mass loss rate, has the mass loss rate changed with time, where is the innermost dust located, what is the size of the dust grains, what is the geometry of the shell?

Numerous papers have been published which addressed one or more of these issues. In many a radiative transfer model is used to model the spectral energy distribution (SED) from which the inner dust radius, the dust optical depth and the luminosity

(for a given distance) are derived. The stellar effective temperature and the grains size (distribution) are often assumed. Table 1 provides a brief summary of the parameters assumed and derived in the various models.

In most cases, spatial brightness distribution observations (visibility curves) are not calculated and compared to observations. At best, full-width half-maximum (FWHM) or 1/e-widths, derived by fitting a Gaussian curve to the visibility curves, are compared to the models. However, a Gaussian curve does not describe the visibility curves very well and, in any case, characterizing the visibility curve by a single number is a loss of information. In this respect, the outline of the present paper is more related to that of Martin & Rogers (1987), Ridgway & Keady (1988), Winters et al. (1994) or Danchi et al. (1994) where visibility curves are calculated using a radiative transfer model and compared directly to observations.

The results of these four papers are quite different, however. Martin & Rogers (1987) find that with an inner dust radius of 4.5 $R_\star$ (or T_c = 1000 K), an r^{-2} density distribution and small grains ($a < 0.1$ μm) they can fit the SED, and the visibility curve at 11 μm. The 2.2 μm visibility curve is not well fitted. Ridgway & Keady (1988) find that with an inner dust radius of 5.0 ± 0.5 $R_\star$ (or T_c = 1100 ± 100 K) and a $r^{-2.3}$ density distribution for $r \leq 10R_\star$ they can reasonably well fit the visibility curve and fluxes at 1.65, 2.2, 3.15, 4.95, 8.4 and 10.3 μm. Scattering was included assuming an albedo without consistently calculating the absorption and scattering coefficients for a given grain size (distribution). The model of Winters et al. (1994) is the most consistent model of all, in the sense that it calculates the formation and growth of dust particles and the velocity structure of the gas and dust, i.e., the density structure is not some power-law but calculated from first principle. They find an inner radius of 1.4 $R_\star$ (or T_c = 1400 K). They fit the SED and the visibility curve at 11 μm. The 2.2 μm visibility curve is not well fitted. To fit the 11 μm visibility curve they had to assume a different distance to IRC +10 216 than that derived to fit the SED! The mass loss rate of 8 × 10^{-5} M$_\odot$ yr^{-1} they propose is much higher than found by other workers, and is in fact higher than the upper limit of 4 × 10^{-5} M$_\odot$ yr^{-1} derived by Keady & Ridgway (1993) from the non-detection of the H$_2$ S(1) rotation line at 17.0 μm. Finally, Danchi et al. (1994) fitted the visibility curve and flux at 11.3 μm at maximum light and derived an inner dust radius of 2.3 $R_\star$ (or T_c = 1360 K) and find an $r^{-1.3}$ density distribution is needed to fit the data. They assumed a power-law distribution of the grain sizes, similar to that of the interstellar medium (ISM).

Clearly there is disagreement over the value of the inner radius, the density law and the grain size.

The aim of the present paper is to re-investigate the properties of the circumstellar shell around IRC +10 216. As constraints the SED from 0.5 to 60000 μm, a 2-4 μm spectrum, two 8-23 μm spectra, visibility curves between 1.6 and 11.3 μm and optical, far-IR and cm sizes will be used.

Although it is well known that the shell around IRC +10 216 is not spherically symmetric (obvious from e.g. visibility curves obtained at various position angles (see later); also see Kastner & Weintraub 1994 (NIR polarimetry), or Le Bertre 1988 (direct imaging)) the model does assume spherical symmetry. This limitation must be kept in mind and will be discussed when appropriate.

The outline of this paper is as follows. In Sect. 2 the model is described and in Sect. 3 the results of the model calculations are presented. We start with presenting the best fitting model with an r^{-2} density distribution and outline the influence of the various parameters, in particular the influence of scattering. Then we consider the effects of a non-constant dust velocity with radius (Sect. 3.2.1), the question of a non-constant mass loss law (Sect. 3.2.2), the effect of molecular line emission (Sect. 3.3) and the effect of free-free emission (Sect. 3.4). The paper ends with discussion and conclusions in Sect. 4. In a separate *Letter* (Groenewegen 1996) the results regarding the free-free emission are discussed more extensively.

2. Model

The calculations are performed with the radiative transfer model of Groenewegen (1993). This model was developed to handle non-r^{-2} density distributions in spherically symmetric dust shells. It simultaneously solves the radiative transfer equation and the thermal balance equation for the dust in spherical geometry, assuming isotropic scattering (i.e. a-symmetry parameter $g \equiv 0$). Some aspects of fitting a SED are repeated here.

The shape of the calculated energy distribution is determined mainly by the shape of the spectrum of the underlying star, the inner dust radius (or equivalently, the temperature of the dust at the inner radius, T_c), and the optical depth. In general the optical depth is given by:

$$\tau_\lambda = \int_{r_{inner}}^{r_{outer}} \pi a^2 Q_\lambda \, n_d(r) \, dr$$

$$= 5.405 \times 10^8 \, \frac{\dot{M} \, \Psi \, Q_\lambda/a}{R_\star \, v_\infty \, \rho_d \, r_c} \int_1^{r_{max}} \frac{R(x)}{x^2 w(x)} \, dx \qquad (1)$$

where $x = r/r_c$, $\dot{M}(r) = \dot{M} \, R(x)$ and $v(r) = v_\infty \, w(x)$. The normalized mass loss rate profile $R(x)$ and the normalized velocity law $w(x)$ should obey $R(1) = 1$ and $w(\infty) = 1$, respectively. In the case of a constant mass loss rate and a constant velocity, the integral in Eq. (1) is essentially unity since r_{max} is always much larger than 1. The symbols and units in Eq. (1) are: the (present-day) mass loss rate $\dot{M}$ in M$_\odot$ yr^{-1}, Ψ the dust-to-gas mass ratio (assumed constant with radius), Q_λ the extinction coefficient, a the grain size in cm (the model assumes a single grain size), $R_\star$ the stellar radius in solar radii, v_∞ the terminal velocity of the dust in km s^{-1}, ρ_d the dust grain specific density in g cm^{-3}, r_c the inner dust radius in units of stellar radii and r_{max} the outer radius in units of r_c.

Unless otherwise specified the outer radius is determined in the model by a dust temperature of 20 K. This corresponds to $r_{max} \sim 7 \times 10^3$. A dust-to-gas ratio of $\Psi = 0.005$ and a grain specific density of $\rho_d = 2.0$ g cm^{-3} are adopted throughout the calculations, unless otherwise specified.

In the model a velocity law of the following form is allowed for

$$w = \frac{v(r)}{v_\infty} = w_0 + (1 - w_0) \left(1 - \frac{R_\star}{r}\right)^\beta \tag{2}$$

with free parameters w_0 and β.

In most models the terminal velocity of the dust is assumed to be equal to that of the gas. This however neglects the drift velocity of the dust with respect to the gas. The terminal velocity of the dust may be estimated from

$$v_\infty = v_\infty^{\text{gas}} + 1.43 \times 10^{-4} \text{ km s}^{-1} \left(\frac{L <Q> v_\infty^{\text{gas}}}{\dot{M}}\right)^{0.5} \tag{3}$$

where v_∞^{gas} is adopted to be 14.5 km s^{-1} (as determined from e.g. CO line profiles), and the second term is the drift velocity, with L the stellar luminosity in solar units and $<Q>$ the flux-averaged extinction coefficient far from the star. From the best fitting models presented later it is found that $<Q> = 0.042$ and $\dot{M} = 2.1 \times 10^{-5} \sqrt{L/15000} \text{ M}_\odot \text{ yr}^{-1}$ are representative values. To estimate v_∞ an estimate for the luminosity is needed. Based on the period-luminosity relation for carbon stars of Groenewegen & Whitelock (1996) a luminosity of about $10000 \text{ L}_\odot$ is predicted for the observed period of 649 days (Le Bertre 1992). As the SED near maximum light will be modeled the default luminosity will be $15000 \text{ L}_\odot$. For $L = 15000 \text{ L}_\odot$ the drift velocity is 3.0 km s^{-1}, and since its value only depends on the $\frac{1}{4}$-th power of L, the terminal velocity of the dust is taken as $v_\infty = 17.5 \text{ km s}^{-1}$ in all calculations. I stress that apart from the estimation of the drift velocity the results in this paper are scalable to arbitrary luminosities.

The spectrum of the central star is represented by a black-body of temperature T_{eff} modified to allow for the characteristic absorption feature in carbon stars near 3.1 μm

$$B_\lambda(T_{\text{eff}}) \exp\left(-A \, e^{-\left(\frac{\lambda - \lambda_0}{\Delta\lambda}\right)^2}\right) \tag{4}$$

with $\lambda_0 = 3.1 \mu$m. Following Groenewegen et al. (1994), $A = 4.605$ and $\Delta\lambda = 0.075 \mu$m are adopted. A value of $A = 4.605$ means that in a star without a circumstellar shell the flux in the feature at 3.1 μm is 1% of the continuum.

For the dust properties a combination of amorphous carbon (AMC) grains and silicon carbide (SiC) grains is assumed. For simplicity, one condensation temperature is used. In principle, SiC and AMC could have different temperature profiles but to take this into account requires two additional free parameters (a second condensation temperature and a second dust-to-gas ratio). Since the abundance of SiC is found to be small, the simplification of the temperature profile appears justified.

Scattering and absorption coefficients are calculated using Mie theory for spherical grains (Bohren & Huffman 1983). For AMC the optical constants of the AC1-species from Rouleau & Martin (1991) are used[1].

---

[1]   The referee pointed out that this soot, since it is produced by striking an arc between two amorphous carbon electrodes in an Argon atmo-
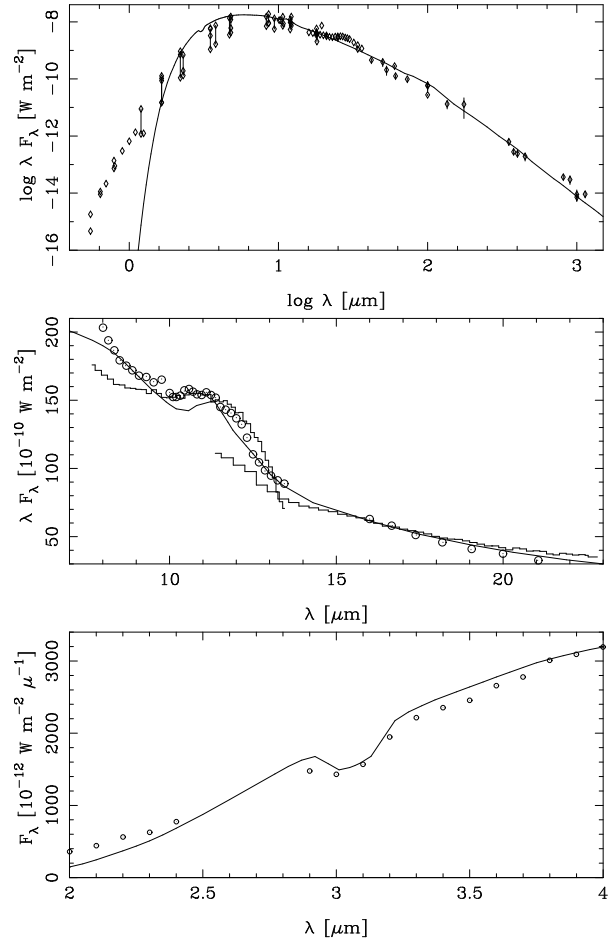
Fig. 1. Model A, the best-fitting model with a r^{-2} density distribution tuned to fit the data near maximum light. In all three panels the solid line represents the model. In the top panel the SED is plotted. The observations are represented by the diamonds. Connected symbols represent data at minimum and maximum light. In the far-IR error bars are plotted. In the middle panel the 7-23 μm spectrum is plotted. The histogram represents the blue and red part of the LRS spectrum The blue part is scaled upwards by a factor of 1.35 to agree with the previous observations of Treffers & Cohen (1974), represented by the circles. The model is scaled to the observations at 16 μm. In the bottom panel the model is compared to the 2-4 μm spectrum of Merrill & Stein (1976), represented by the circles. The model is scaled to the observations at 4 μm. Both for the Merrill & Stein and the Treffers & Cohen spectra the flux values were read of their respective figures for discrete wavelengths only. The scaling in absolute flux terms is needed to account for the stars variability.

In Groenewegen (1995) several types of silicon carbide were compared to observed LRS spectra of carbon stars and it was concluded that α-SiC (Pégourié 1988) gave the best fit in the majority of cases. The optical constants for this SiC species are therefore used. The optical constants ($m \equiv n - ik$) are extrapolated to longer wavelengths than that given by the respective

---

sphere, is likely to contain only a small fraction of Hydrogen, contrary to what is expected for carbon grains formed in the Hydrogen-rich circumstellar shell of IRC +10 216.

authors assuming an $\lambda^{-\alpha}$ dependence for n and k. The total scattering and absorption coefficients are calculated from $Q_\lambda = x\,Q_\lambda{}^{\text{SiC}} + (1-x)\,Q_\lambda{}^{\text{AMC}}$ where x ($\in [0,1]$) is determined by the fit to the observed 11.3 μm SiC feature.

A few additional steps are necessary to compare the calculated with the observed energy distribution. The models are corrected for an assumed interstellar extinction of $A_{\text{V}} = 0.1$, consistent with the location of IRC +10 216 at 45 degrees from the galactic plane and its distance of less than 300 pc (limited by the theoretical maximum luminosity of an AGB star). Interstellar extinction at other wavelengths is calculated using Cardelli et al. (1989).

Beam effects are taken into account. This is especially important for longer wavelengths ($\lambda \gtrsim 50\,\mu$m) where the emission becomes extended relative to the typical beams used in far-infrared observations. In particular, for $\lambda < 7\,\mu$m a Gaussian beam with a FWHM (full width half maximum) of $20''$ is assumed (typical of near-infrared observations). Between 7 μm $< \lambda < 140\,\mu$m the beam effects of the IRAS detectors is taken into account (For details see Groenewegen 1993). For $\lambda > 140$ μm a Gaussian beam of FWHM = $84''$ is assumed, representative of the far-IR observations the model is compared to.

In the models the calculated energy distribution is convolved with the spectral response of the IRAS filters (Table II.C.5 of the Explanatory Supplement) to compare the predicted flux-densities directly to the flux-densities listed in the Point Source Catalog.

The observations to which the calculated SEDs are compared are listed in Table 2. The entries are the wavelength, the flux, the beam width (when applicable) and the phase of the observations are listed. The LRS spectrum has been corrected following Cohen et al. (1992), and the blue part has been multiplied by a factor of 1.35 to agree with the spectrum of Treffers & Cohen (1974) at 11.3 μm. Table 2 does not include the cm-observations (see Table 7) and some recent far-IR data obtained with IRAM and JCMT (Walmsley et al. 1991, Marshall et al. 1992, Althenoff et al. 1994, van der Veen et al. 1995), telescopes which have beams of 11 and $18''$ in the far-IR, respectively, and clearly resolve the far-IR emission (these observations will be discussed in Table 6, Sect. 3.2.2 and 3.4).

2.1. Visibility curves

The most important change with respect to the original 1993 model version is the possibility to calculate the so-called visibility curves. An excellent introduction on this topic can be found in Bracewell (1986). Briefly, the visibility curve is defined as the Fourier transform of the intensity distribution $I(x,y)$

$$F(u,v) = \int_{-\infty}^{\infty} \int_{-\infty}^{\infty} I(x,y)e^{-i\,2\pi(ux+vy)}\,dx\,dy \qquad (5)$$

which in the case that the intensity is a function of $p = \sqrt{x^2 + y^2}$ (i.e. circular symmetry) simplifies to the Hankel transform ($q = \sqrt{u^2 + v^2}$)

$$F(q) = 2\pi \int_0^{\infty} I(p)J_0(2\pi qp)p\,dp \qquad (6)$$

where J_0 is the zero-th order Bessel function. The visibility is then defined as

$$V(q) = \sqrt{F^2(q)}/F(0) \qquad (7)$$

Eq. (6) is solved numerically for 100 equidistant values of q between 0 and 6 arcsec^{-1} following Rogers & Martin (1984) by dividing the integral in 16 about equal subintervals, on each of which a 20-point Gaussian quadrature is employed using a polynomial approximation for J_0 (Abramowitz & Stegun 1972) and a spline approximation for $I(p)$.

The observations to which the models are compared are listed in Table 3. Dr. Danchi provided the data in computer readable form, the other data was obtained by scanning the relevant figures in the original publications.

To conclude the description of the model, it is recalled that due to the modeling approach both the calculated SED and visibility curves are invariant under a change in the assumed distance D, *IF* the mass loss rate is changed as $\dot{M} \sim D$, and the luminosity as $L \sim D^2$ (and all other parameters remain unchanged). This follows since, obviously, L/D^2 ($\sim$ observed total flux at earth) = constant, hence $R_\star/D$ ($\sim$ angular size) $\sim \sqrt{L/T_{\text{eff}}^4}/D$ = constant and (see Eq. 1) $\tau \sim \dot{M}/R_\star \sim D/\sqrt{L}$ = constant.

3. Results of the calculations

3.1. Models with a r^{-2} density distribution

To get a feeling for the sensitivity of the results on the parameters optical depth, effective temperature and inner dust radius the possible complicating factors of a non-constant velocity law and a non-constant mass loss rate are ignored for the moment. These issues will be addressed in Sects. 3.2.1 and 3.2.2. All models discussed below are tuned to fit the observations at maximum light as most of the available data is taken near maximum light.

A grid of models was run varying $T_{\text{c}} = 900, 1000, 1050, 1100, 1300$ and 1500 K, $T_{\text{eff}} = 1800, 2000$ and 2400 K, and $\dot{M} = 1.2, 1.6, 2.0, 2.4$ and 2.8×10^{-5} M$_\odot$ yr^{-1} with the grain size fixed at 0.16 μm. The ratio SiC/AMC was determined to be 0.03 by fitting the SiC feature in the 7-20 μm spectra. For this particular choice the opacities ($\kappa_\lambda \equiv 3Q_\lambda^{\text{ext}}/(4a\rho_{\text{d}})$) at 11.33 and 60 μm are $\kappa_{11.33\mu m} = 624$ cm^{2}g^{-1} and $\kappa_{60\mu m} = 68$ cm^{2}g^{-1} for the adopted specific grain density of 2.0 g cm^{-3}.

In Fig. 1 the best fitting model is compared to the observed SED, the observed 2-4 μm spectrum and observed 8-23 μm spectra. In Fig. 2 the best fitting model is compared to the visibility data. The model parameters are listed in Table 3 (model A). Note the grain size of 0.16 μm. The radius of the central star in this model is 35.1 mas.

Several things may be remarked. Beyond $\approx 2\,\mu$m the SED is well fitted. For shorter wavelengths the model falls increasingly short of the observations. The origin of this will be discussed later. The observed flux short ward of 2 μm contributes less than 0.1% to the total flux so that this discrepancy does not influence the estimate for the luminosity in any way. Based on a comparison of predicted and observed magnitudes near

Table 4. Model parameters

Model	$T_{\rm eff}$ (K)	τ at 11.33μm	$r_{\rm c}$ ($R_\star$)	$T_{\rm c}$ (K)	a (μm)	$\dot{M}^{\rm (a,b)}$ (M$_\odot$/yr)	$L^{\rm (b)}$ (L$_\odot$)	discussed where	remarks
A	2000	0.621	4.47	1075	0.16	2.2 (-5)	15000	Sect. 3.1; Figs. 1&2 solid line	Best-fitting r^{-2} model
B	2000	0.579	4.83	1075	0.20	2.2 (-5)	15000	Sect. 3.1.1; Fig. 3 solid line	
C	2000	0.679	4.06	1075	0.12	2.2 (-5)	15000	Sect. 3.1.1; Fig. 3 dash-dotted line	
D	2000	0.772	3.56	1075	0.05	2.2 (-5)	15000	Sect. 3.1.1; Fig. 3 dotted line	
E	2000	0.469	4.31	1075	0.16	1.6 (-5)	15000	Sect. 3.1.2; Figs. 4&5 solid line	
F	2000	0.766	4.61	1075	0.16	2.8 (-5)	15000	Sect. 3.1.2; Figs. 4&5 dotted line	
G	1700	0.699	2.87	1075	0.16	2.2 (-5)	15000	Sect. 3.1.3; Fig. 6 solid line	
H	2300	0.560	6.57	1075	0.16	2.2 (-5)	15000	Sect. 3.1.3; Fig. 6 dotted line	
I	2000	0.477	5.81	950	0.16	2.2 (-5)	15000	Sect. 3.1.4; Figs. 7&8 solid line	
J	2000	0.773	3.59	1200	0.16	2.2 (-5)	15000	Sect. 3.1.4; Figs. 7&8 dotted line	
K	2000	1.129	4.85	1075	0.16	2.2 (-5)	15000	Sect. 3.2.1; Figs. 9&10 solid line	velocity law
L	2000	0.843	4.61	1075	0.16	1.5 (-5)	15000	Sect. 3.2.1; Figs. 9&10 dash-dotted line	velocity law
M	1800	1.044	4.17	1000	0.16	1.9 (-5)	15000	Sect. 3.2.1; Figs. 9&10 dotted line	velocity law
N	2000	0.621	4.47	1075	0.16	(c)	15000	Sect. 3.2.2	$\dot{M} \neq 0$
O	2000	0.621	4.47	1075	0.16	(d)	15000	Sect. 3.2.2	$\dot{M} \neq 0$
P	2000	0.621	4.47	1075	0.16	(e)	15000	Sect. 3.2.2	$\dot{M} \neq 0$
Q	2000	0.621	4.47	1075	0.16	(f)	15000	Sect. 3.2.2	$\dot{M} \neq 0$
R	2000	0.621	4.47	1075	0.16	(e)	15000	Sect. 3.4	$\dot{M} \neq 0, Q_\lambda$

[a] a (-b) stands for $a \times 10^{-b}$. A dust-to-gas ratio of 0.005 is assumed to convert the dust mass loss rate into a gas mass loss rate.
[b] Values for $\dot{M}$ and L are given for a distance of 135 pc. For other distances, the mass loss rates and luminosity scale like $\dot{M} \sim D$ and $L \sim D^2$, respectively. The other parameters are independent of the assumed distance.
[c] A mass loss rate of 2.2×10^{-5} M$_\odot$/yr for $r < 27''$ and a factor 4 larger for $r > 27''$.
[d] A mass loss rate of 2.2×10^{-5} M$_\odot$/yr for $r < 82''$ and a factor 6 larger for $r > 82''$.
[e] A mass loss rate of 2.2×10^{-5} M$_\odot$/yr for $r < 123''$ and a factor 9 larger for $r > 123''$.
[f] An exponentially decreasing mass loss rate (see Sect. 3.2.2).

maximum light in the M, N, N1, N2, N3 filters and IRAS 12 μm band (covering the wavelength region where most of the flux is emitted) it is estimated that the derived luminosity of 823 000 L$_\odot$kpc^{-2} at maximum light (corresponding to an observed flux at earth of 2.53×10^{-8} W m^{-2}) is accurate to within 5%.

The available 8-23 μm spectra are very well fitted. This part of the spectrum is sensitive to the optical depth (influencing the slope of the spectrum) and the amount of SiC. The model shown has 3% SiC and fits the feature reasonably well.

The observed 2-4 μm spectrum is very well fitted. This part of the spectrum is sensitive to the optical depth (influencing the slope of the spectrum), the temperature at the inner radius (since dust of $\sim$1000 K radiates predominantly in this wavelength region) and the strength of the 3.1 μm feature. It is recalled that a strong 3.1 μm feature is assumed in the central star (the observed feature will be less strong due to dust emission). This means, within the simplified approach adopted here, that a feature which is predicted to be weaker than observed can not be accounted for in the model, while a feature that is stronger than observed can always be made in agreement by reducing the parameter A in Eq. (4).

In Fig. 2 the visibility data are compared to the model. One immediately notes that the observations reveal the a-symmetry of the envelope, especially at K and L (for details see the figure caption). The models were tuned to go roughly halfway between the extreme data points. The visibility data is fitted quite well. It is shown below that the K-band visibility data is very sensitive to the grain size. Note that at 11 μm the model has a steeper decline than the observations. Since the error bars on the observations are smaller than the size of the plot symbols, this effect is real. This could indicate a density law which is shallower than r^{-2}. From their 11.15 μm visibility data, Danchi et al. (1994) derived a $r^{-1.5}$ density law.

In the following subsections the influence of the various parameters is investigated.

3.1.1. Influence of scattering

Two constrains are used to determine the grain size and the effect of scattering: (A) the visibility curves and (B) the sizes of the shell in optical images as observed by Le Bertre (1988). Le Bertre determined the size of the shell in Gunn g, r, i, z filters for position angles (PA) = 0, 45, 90 and 135° near maximum light (phase = 0.08) under good seeing conditions. For all four filters, the FWHM for PA = 0 was the largest, followed by the values for PA = 135, 45 and 90°. The range in the deconvolved FWHM values are listed in Table 5. For model A the values fall just short of, or are in agreement with, the lowest observed values.

In Fig. 3 the SED and K and L-band visibility data are shown for grain sizes of 0.20, 0.12 and 0.05 μm (Models B, C and D
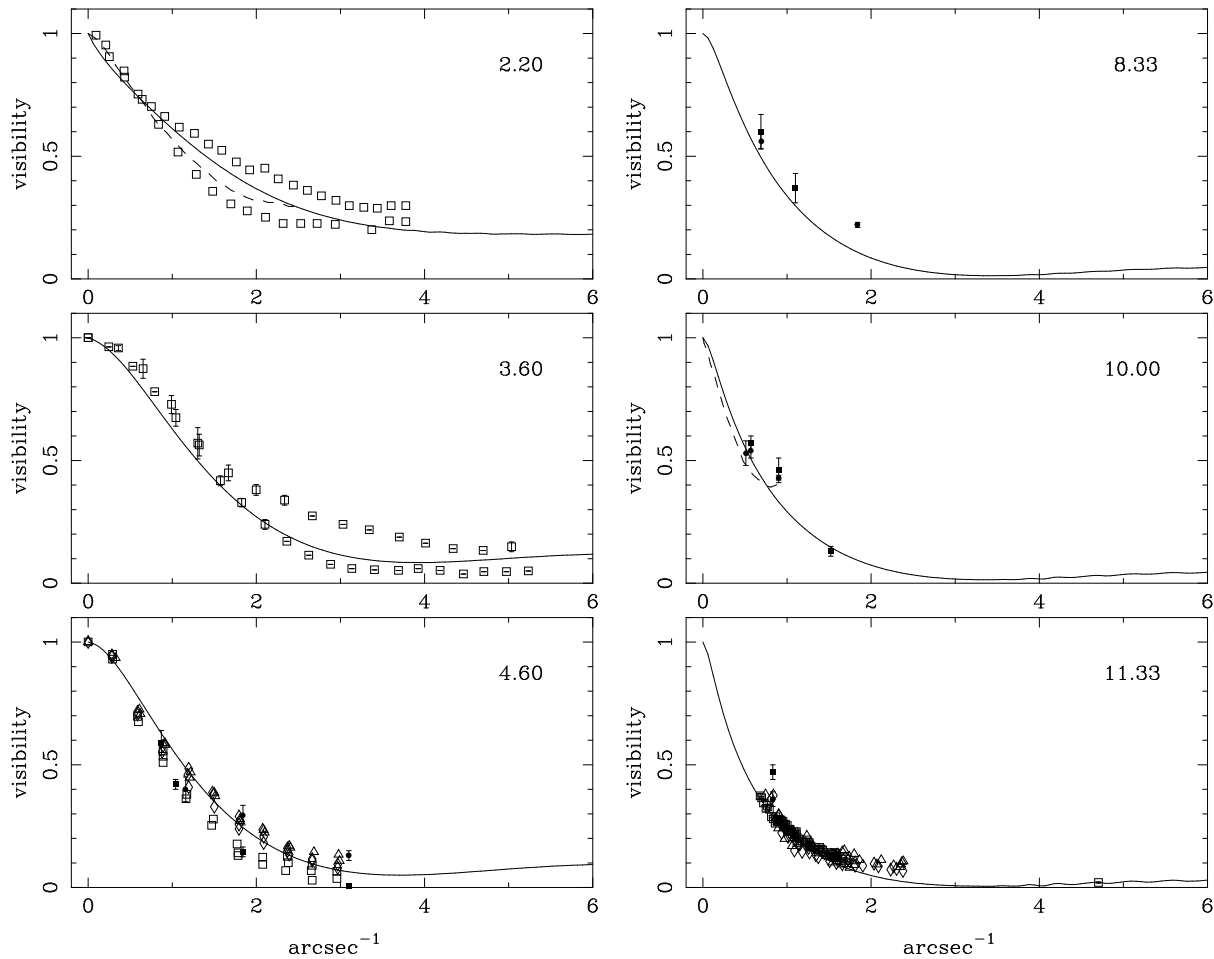
Fig. 2. Model A, the best-fitting model with a r^{-2} density distribution. In all panels the solid line represents the model. The number in the upper right corner of each panel indicates the wavelength in micron for which the model was calculated. The data are as follows: upper left panel: squares: Dyck et al. (1984) at 2.2 μm and phase of observation $\phi = 0.91$, the higher visibilities represent the E-W scan, the lower visibilities the N-S scan; dashed line: Dyck et al. (1987) at 2.2 μm and $\phi = 0.06$, average over 4 position angles. Middle left panel: Mariotti et al. (1983) at 3.5 μm and $\phi = 0.54$, the upper curve is for PA = 90, the lower curve for PA = 150°. Error bars are plotted when larger than the symbol size. Lower left panel: Mariotti et al. (1983) at 4.6 μm and $\phi = 0.54$ for PA = 0 (open squares), 60 (open diamonds), 120° (open triangles). Filled symbols (squares PA = 0, circles PA = 90) come from McCarthy et al. (1980) at 5.0 μm at various phases. Upper right panel: McCarthy et al. (1980) at 8.4 μm and various phases. Filled squares (PA = 0), filled circles (PA = 90). Middle right panel: McCarthy et al. (1980) at 10.2 μm and various phases. Filled squares (PA = 0), filled circles (PA = 90). The dashed line represents the data from Dyck et al. (1987) at 10.3 μm and $\phi = 0.84$ and is an average over 6 position angles. Bottom right panel: Danchi et al. (1994) at 11.15 μm around maximum light (open squares); Sutton et al. (1979) at 11.11 μm; diamonds represent the data set 'west of meridian' (around maximum light), triangles the data set 'east of meridian' (around $\phi = 0.4$). Filled square (PA = 0) and filled circle (PA = 90) come from McCarthy et al. (1980) at 11.1 μm and $\phi = 0.5$.

respectively. All other parameters are equal to that of model A). The model for $a = 0.05$ μm is shown since this is a typical grain size adopted in many previous models. The 2-4 and 8-23 μm spectra and the visibility curves at longer wavelengths are not shown since they are not markedly different from those shown in Figs. 1 and 2. The effect of scattering on the K-band visibility data is very strong. In particular the slope of the visibility curve for small spatial frequencies is sensitive to the grain size, and allows the best fitting grain size of 0.16 μm to be determined quite accurately. The effect on the L-band visibility is already much less. From Fig. 3 one can estimate that the L-band visibility is sensitive to grains larger than $\gtrsim 0.18$ μm and the K-band

visibility data to grains larger than $\gtrsim 0.05$ μm. Note that grains of size 0.05 μm provide a much better fit to the SED, but simply fail to fit the K-band visibility and the optical sizes (Table 5). When scattering is essentially absent the FWHM of the optical surface brightness profiles is simply the stellar diameter (70.3 mas). Even the model with $a = 0.12$ μm gives optical sizes significantly below the observed ones beyond ~ 0.6 μm. Based on the optical sizes and the K-band visibility curve a dominant grain size of between 0.14 and 0.18 μm is derived.
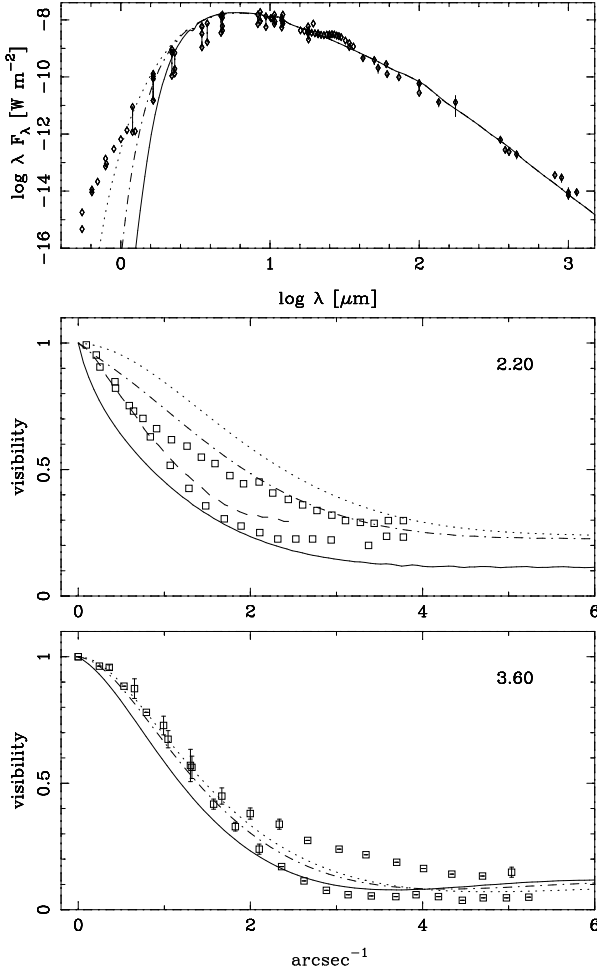
Fig. 3. Influence of grain size, c.q. scattering, on the SED and the K and L-band visibility curve. Models with $a = 0.20$ μm (model B, solid line), 0.12 (model C, dash-dotted line), 0.05 (model D, dotted line). The effect of the grain size is most clearly seen in the K-band visibility curve.

3.1.2. Influence of optical depth

Figs. 4 and 5 show the influence of the mass loss rate on the SED, spectra and visibility curves (models E and F with mass loss rates of 1.6 and 2.8 $\times$ 10^{-5} M$_\odot$ yr^{-1}, respectively). The lower (higher) mass loss rate results in bluer (redder) spectra and this is particular obvious in the 2-4 and 8-20 μm spectra. The optical sizes (Table 5) of model E are not in agreement with observations, those of model F are in better agreement with observations than those of model A.

Regarding the visibility curves, the higher mass loss rate results in lower visibilities. This reflects the increase of dust emission relative to that of the central star. The effect is smaller for longer wavelengths where the shell already dominated the stellar emission in model A.

The lower mass loss rate model fits the L-band visibility better than model A. The higher mass loss rate model fits the M-band and the K-band visibility at small spatial frequencies better than model A. Both models however fail to reproduce
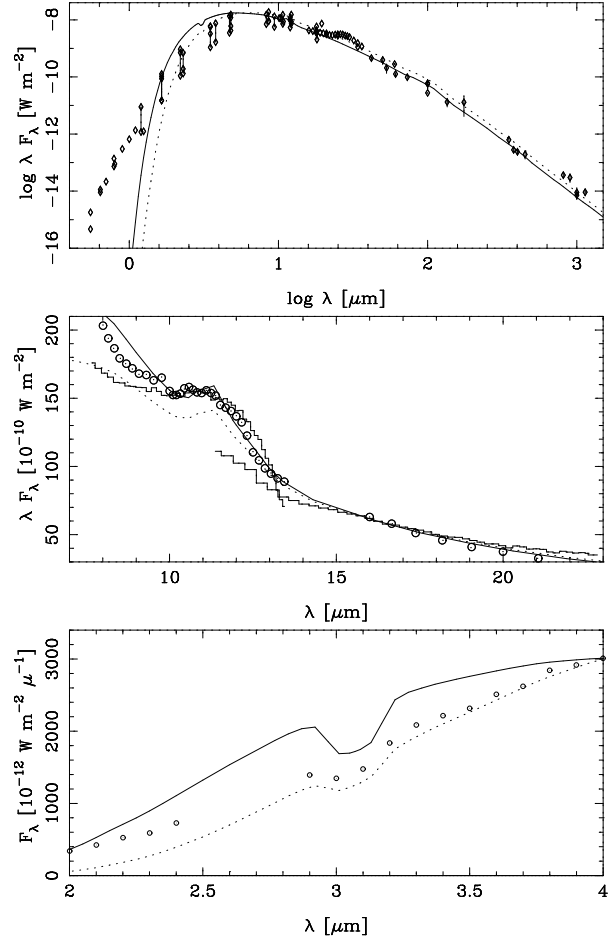
Fig. 4. Influence of optical depth. Models E (solid line; $\dot{M} = 1.6 \times 10^{-5}$ M$_\odot$ yr^{-1}) and F (dotted line; $\dot{M} = 2.8 \times 10^{-5}$ M$_\odot$ yr^{-1}).

the 2-4 and 8-20 μm spectra, and model E fails to predict the optical sizes. As a compromise to fit all constraints the best fit is obtained with $\dot{M} = 2.2 \times 10^{-5}$ M$_\odot$ yr^{-1}.

3.1.3. Influence of $T_{\rm eff}$

Fig. 6 illustrates the effect of changing the effective temperature of the central star to $T_{\rm eff} = 1700$ (model G) or 2300 K (model H). The cooler central star model is slightly redder (a combined effect of a slightly larger optical depth and an intrinsically redder central star) but the effect on the SED (as on the 2-4 and 8-20 μm spectra) is small. With all parameters equal, the stellar radius varies as $\sim T_{\rm eff}^{-2}$ and the inner dust radius, in the optically thin case and for $Q_\lambda \sim \lambda^{-1}$, appropriate for AMC dust, as $r_{\rm c} \sim T_{\rm eff}^{2.5}$. Hence, to first order, $\tau \sim T_{\rm eff}^{-0.5}$.

The changes in the visibility curve are relatively larger. The reason is the larger inner radius in terms of the stellar radius. The signature for larger inner radii is a relative low visibility at small spatial frequencies and relative large visibility at larger spatial frequencies.
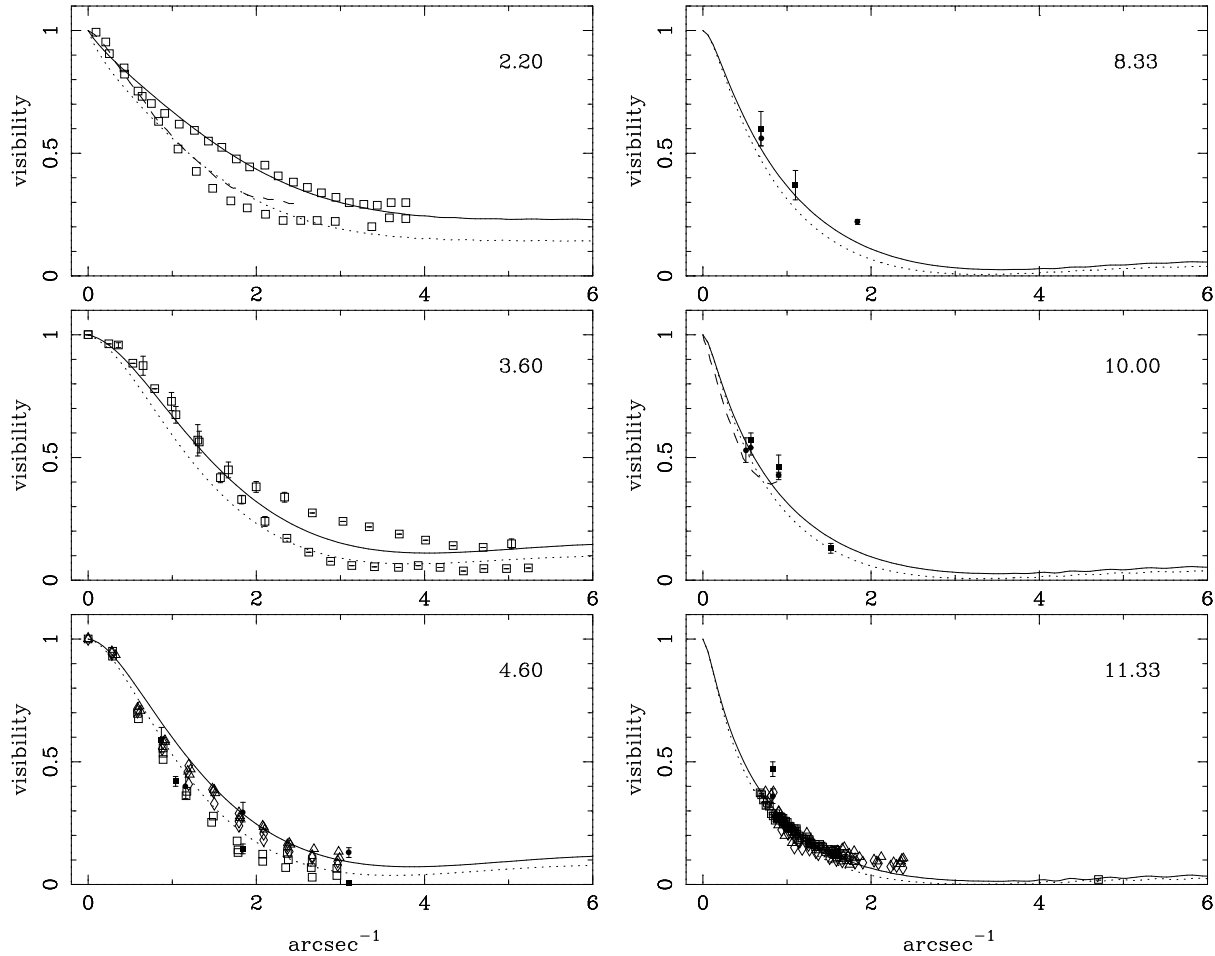
Fig. 5. Influence of optical depth. Models E (solid line; $\dot{M} = 1.6 \times 10^{-5}$ M$_\odot$ yr^{-1}) and F (dotted line; $\dot{M} = 2.8 \times 10^{-5}$ M$_\odot$ yr^{-1}).

3.1.4. Influence of T_c

Figs. 7 and 8 illustrate the effect of changing the inner dust temperature to 950 K (model I), or 1200 K (model J). The changes in the predicted strength of the 3.1 μm feature are striking. Model J just fits the observed feature. Models with even larger T_c do not. This is due to the increase in dust emission at short wavelengths with increasing T_c. The same effect causes the K-band visibility not to match the observations. The dust emission compared to the stellar emission is too large. The model with $T_c = 950$ K does not fit the visibility data since the inner radius is too large. Nor does this model fit the optical sizes.

3.1.5. Summary

To summarize the results of the models with a r^{-2} density law it is found that the following range of parameters can account for all constraints considered here (optical sizes, visibility curves, SED, 2-4 and 8-20 μm spectra): Luminosity at maximum light 15000 $\pm$ 750 L$_\odot$, dust mass loss rate 1.1 $\pm$ 0.1 $\times$ 10^{-7} M$_\odot$ yr^{-1}, grain size 0.16 $\pm$ 0.01 μm, effective temperature $T_{\rm eff}$ = 2000 $\pm$ 100 K, inner dust temperature T_c = 1075 $\pm$ 50 K, inner dust radius r_c = 4.5 $\pm$ 0.5 $R_\star$. Error bars represent estimated 1σ

values. The mass loss rate and luminosity are based on an assumed distance of 135 pc but are easily scaled to other distances ($L \sim D^2$; $\dot{M} \sim D$). The other parameters are independent of distance. There is an additional (external) uncertainty in the dust mass loss rate due to the uncertainty in the adopted dust velocity (5%), and, more importantly, in the absolute value of the dust opacity (possibly up to a factor of 3).

Regarding the determination of the grain size it is emphasized that none of the parameters discussed above is as sensitive to the shape of the visibility curve for spatial frequencies $\lesssim 1.5$ arcsec^{-1} as the grain size. This allows an accurate determination of the grain size. This property makes it possible to derive the dominant grain size in the shells of other AGB stars as well, provided that near-IR visibility curves are available.

It is also shown that fitting the SED *per se* would lead one to believe that small grains are predominant in the shell around IRC +10 216.

Table 5. Comparison of calculated and observed optical sizes

λ (μm)	0.52 μm	0.69 μm	0.82 μm	0.92 μm
Observed	0.65-1.30″	0.71-1.18	0.63-1.15	0.60-0.99
Model				
A	0.63″	0.78	0.67	0.57
B	0.25	0.72	0.81	0.78
C	0.64	0.52	0.37	0.07
D	0.07	0.07	0.07	0.07
E	0.47	0.62	0.54	0.37
F	0.71	0.93	0.79	0.67
G	0.62	0.77	0.67	0.57
H	0.61	0.77	0.66	0.51
I	0.38	1.28	0.72	0.07
J	0.46	0.60	0.58	0.53
K	0.81	0.93	0.76	0.65
L	0.50	0.63	0.58	0.52
M	0.83	0.91	0.74	0.63
N-R	0.63	0.78	0.67	0.57

Observed data are deconvolved FWHM values in arc seconds determined by fitting Gaussian curves to optical images in Gunn g, r, i, z filters (Le Bertre 1988). The range in FWHM values indicates the measurements at different position angles. Parameters for models A-R are listed in Table 4. Model values are FWHM values determined from the surface brightness profiles.

3.2. Models with a non-r^{-2} density distribution

3.2.1. Influence of a non-constant velocity law

In Sect 3.1 a constant velocity law was assumed in the calculations (Eq. (2) with $\beta \equiv 0$). In reality the dust velocity will increase from a small to its terminal value. This means that close to the star the density structure could be steeper than a r^{-2} law. This could influence the shape of the SED, and the visibility curves. A complicating factor is that the dust-to-gas mass ratio will *also* increase with radius from zero to its final value. Since the optical depth depends on $\frac{\Psi}{v}$ (see Eq. 1) the net effect could be small. In this subsection the effect of a steeper density law near the inner radius is investigated by approximately taking the dust velocity profile into account.

Under the assumption that radiation pressure on dust is responsible for driving the outflow Habing et al. (1994) have solved the momentum equations for the gas and the dust (also see Netzer & Elitzur 1993). For a given set of parameters (stellar mass, luminosity, effective temperature, dust properties, inner dust radius, assumed dust velocity at the inner radius, mass loss rate, dust-to-gas ratio [assumed constant with radius]) the model calculates the gas and dust velocity as a function of radius (for details see Habing et al. 1994).

In principle, one could use this model as an additional constraint on the properties of the circumstellar shell of IRC +10 216 by determining those sets of parameters that result in the calculated terminal velocity of the gas to equal the observed value of 14.5 km s^{-1}. Such a study is beyond the scope of this paper. Instead, I use their code (kindly provided to me by Prof. Habing) to calculate a representative run of the dust velocity
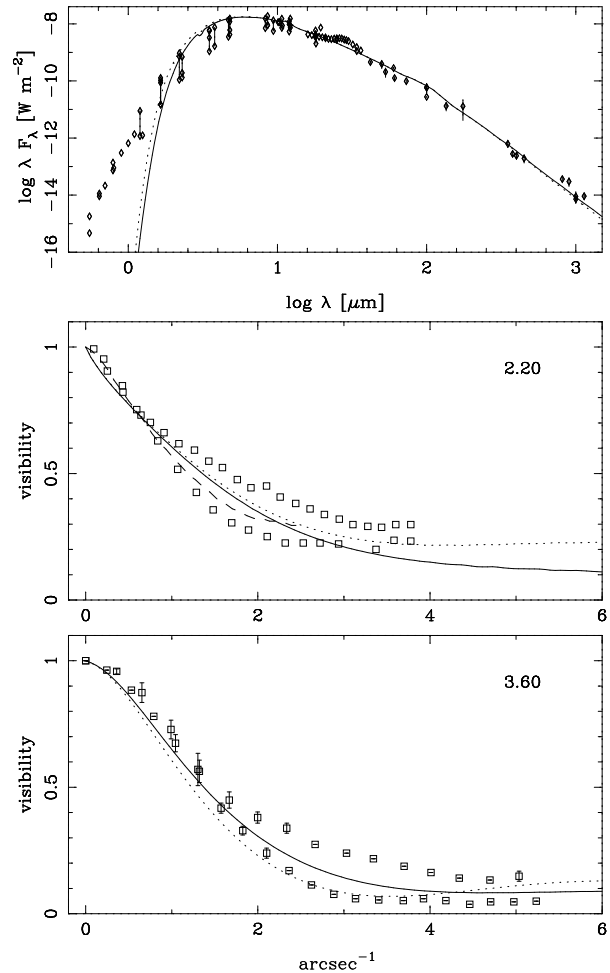
Fig. 6. Influence of the effective temperature on the SED and the K and L-band visibility curve. Models with $T_{\rm eff} = 1700$ K (model G, solid line) and $T_{\rm eff} = 2300$ K (model H, dotted line).

with radius. Assuming a stellar mass of 2 M$_\odot$ and an initial dust and gas velocity at the inner radius of 3.1 km s^{-1}, I ran some models taking the parameters from model A but varying the parameters as well. A least-square fit was made to the calculated dust velocity profile to determine w_0 and β. I typically find $w_0 = 0.01$ and $\beta = 3$. These values will be used in all following calculations. As a matter of interest it is noted that it proved quite difficult to actually find a model that predicts the observed terminal velocity of the gas of 14.5 km s^{-1} and with model parameters that are not in conflict with those derived in Sect. 3.1. In general models with a lower luminosity and a lower dust-to-gas ratio than assumed in Sect. 3.1 are needed.

Model K shows (Figs. 9 and 10) the results of a calculation with the parameters of model A but with the velocity profile included. This model fits the data less well than model A, in particular the visibility data. The primary reason is that the optical is much larger now. Taking into account the different inner dust radii one finds that $\int_1^{r_{\rm max}} \frac{1}{x^2 w(x)} \, dx = 2.0$. In Model L the mass loss rate is lowered from 2.2 to 1.5×10^{-5} M$_\odot$ yr^{-1}. This clearly improves the fit to the visibility curves, but the slope of
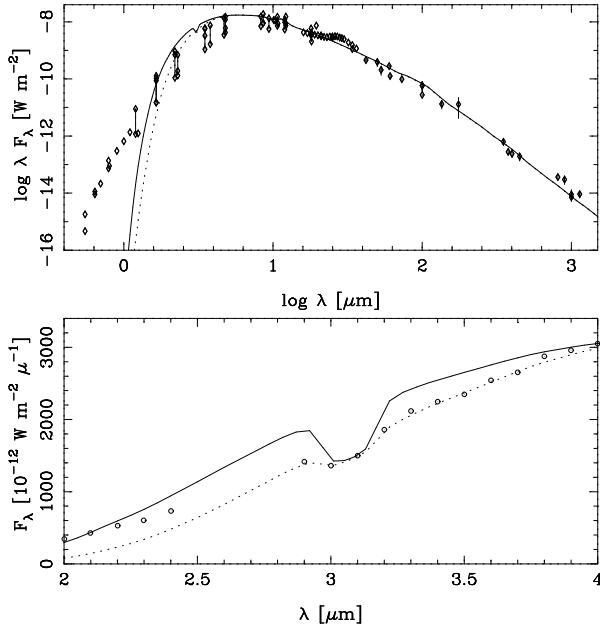
Fig. 7. Influence of the temperature at the inner shell. Models I (solid line; T_c = 950) and J (dotted line; T_c = 1200).

the LRS spectrum is less well fitted. The K- and L-band visibility data are sensitive to the density close the the star while the 11 μm region traces regions further from the star. Lowering the mass loss rate to improve the visibility data will make the slope of the LRS spectrum bluer. I also tried to find a new optimum fit by varying all parameters and the result is model M. This model has a lower effective temperature and lower inner dust temperature. This model appears to fit about equally well as model A. The model parameters are within 2σ of those of model A and so one may argue that the effect of including the dust velocity law is small.

Looking in more detail, model M fits the data slightly worse then model A. In particular, the slopes of the 2-4 and 8-20 μm spectra are less well simultaneously fitted than with a r^{-2} density distribution. In any case, it is clear that the physically more realistic case of including the effect of the dust velocity on the density distribution does not significantly improve the fit to the data in any way.

As mentioned before, the dust-to-gas ratio is expected to increase as well with radius and the two effects tend to cancel. Calculations that take the formation and growth of dust grains and the velocity of the gas and dust into account appear to confirm this. In the thesis of Winters (1994, his Fig. 4.2) one can see how both the dust-to-gas ratio (represented by f_c, the degree of condensation) and the velocity reach 90% of their terminal value at $\sim$10 $R_\star$ in a model where the dust formation starts at 2 $R_\star$. However, the ratio of the dust-to-gas ratio and the velocity is constant to with 5% from 3.6 $R_\star$ outwards (Winters 1995, private communication), implying that a r^{-2} density law may be a good approximation (if $\ddot{M}$ = 0) except very near the inner dust radius.
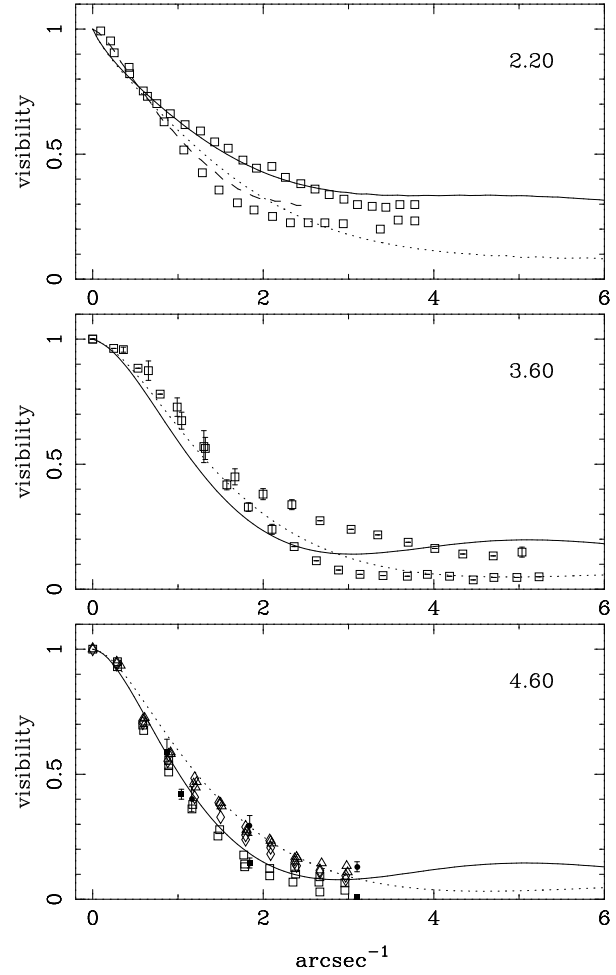
Fig. 8. Influence of the temperature at the inner shell. Models I (solid line; T_c = 950) and J (dotted line; T_c = 1200).

3.2.2. Influence of a non-constant mass loss rate

As mentioned in Sect. 3.1 the difference between the observed and calculated visibility curve at 11.3 μm may indicate a density distribution shallower than r^{-2} far from the star. Danchi et al. (1994) find that a $r^{-1.5}$ density distribution fits their data. Fazio et al. (1980) found that a distribution of the type $(1 + r/25'')/r^2$ could fit their measured angular size at 61 μm. Additional evidence that the mass loss rate was higher in the past comes from CO rotational line emission (Sahai 1987, Truong-Bach et al. 1991).

The following constrains are used to investigate any possible variations of the mass loss rate with time: (A) the visibility curves, in particular beyond 9 μm, (B) the observed (on-source) far-IR fluxes, (C) the observed far-IR fluxes at off-set positions (Walmsley et al. 1991, van der Veen et al. 1995), (D) the observed size at 61 μm of 78 $\pm$ 6$''$ in a 55 $\pm$ 4$''$ beam (Fazio et al. 1980), (E) the deconvolved size at 100 μm of 4.6 $\pm$ 0.3$'$ (Young et al. 1993).

Of these constraints, only the NIR visibility curves and the FIR size are direct tracers of the density structure. The fluxes

Table 6. Model and observations in the far-infrared

Entry[a]	What? [b]	λ (μm)	aperture ($''$)	Observed value	Model A	N	O	P	Q	R
1	FWHM size	61	decon.	$55 \pm 9''$	$17''$	59	62	53	35	53
2	FWHM size	100	decon.	$276 \pm 18''$	$49''$	112	197	282	311	282
3	S(0)	53	84	$3.7 \pm 1.3\ 10^3$ Jy	5823	8027	6116	5904	6275	5904
	S(0)	61	78	$2.6 \pm 0.3\ 10^3$ Jy	4382	6284	4663	4473	4764	4473
	S(0)	100	84	$2.0 \pm 0.7\ 10^3$ Jy	1755	3037	2085	1909	2016	1909
	S(0)	175	84	754 ± 514 Jy	450	869	594	534	549	534
	S(0)	350	84	73 ± 19 Jy	72.7	157	111	98.1	97.1	98.1
4	S(0)	377	86	35 ± 6.6 Jy	55.9	116	80.9	72.6	72.8	72.6
	S(0)	811	86	9.8 ± 1.6 Jy	5.07	10.3	7.43	6.73	6.69	6.73
	S(0)	1136	86	3.5 ± 0.9 Jy	1.77	3.46	2.55	2.33	2.31	2.42
5	S(0)	400	37	32 ± 8 Jy	30.2	42.4	33.7	32.7	33.9	32.7
	S(0)	450	47	29 ± 9 Jy	23.4	36.8	27.4	26.2	27.1	26.2
	S(0)	900	47	9 ± 3 Jy	2.76	4.20	3.22	3.10	3.17	3.10
6	S(0)	761	18.2	5.9 ± 0.4 Jy	2.90	3.23	3.01	2.98	3.05	2.98
	S(0)	1100	18.2	2.23 ± 0.05 Jy	1.00	1.10	1.04	1.03	1.04	1.06
	S(10)/S(0)	1100	18.2	0.58 ± 0.04	0.52	0.57	0.54	0.53	0.54	0.53
	S(20)/S(0)	1100	18.2	0.17 ± 0.02	0.13	0.22	0.16	0.15	0.15	0.15
7	S(0)	1000	60	3.0 ± 1.3 Jy	2.18	3.68	2.71	2.57	2.61	2.57
	S(0)	1000	60	2.4 ± 0.6 Jy	2.18	3.68	2.71	2.57	2.61	2.57
8	S(0)	1300	11	2.550 ± 0.003 Jy	0.55	0.57	0.56	0.56	0.56	0.58
	S(10)/S(0)	1300	11	0.31 ± 0.002^c	0.19	0.22	0.20	0.20	0.20	0.20
	S(20)/S(0)	1300	11	0.06 ± 0.001^c	0.038	0.079	0.050	0.047	0.049	0.050

[a] References to the different entries: 1 = Fazio et al. (1980); 2 = Young et al. (1993). FWHM size at 100 μm as determined by me from their Fig. 20 (the 60 μm data is judged unreliable by them); 3 = Fazio et al. (1980); 4 = Phillips et al. (1982); 5 = Sopka et al. (1985); 6 = van der Veen et al. (1995); 7 = Elias et al. (1978); 8 = Walmsley et al. (1991).
[b] Nomenclature: S(y) means the flux measured at off-set position y''.
[c] Error bars on the flux-ratios have been estimated by me based on the quoted error bar on the on-source flux and assuming an equal observation time spent on the on- and off-source position and a noise level proportional to the square root of the flux.

beyond $\sim$800 μm are not only sensitive to the density structure but also to the possible contribution of free-free emission, the significant contribution of molecular line emission to the broad band fluxes (e.g. Groesbeck et al. 1994) and the uncertainty in the long-wavelength dependence of the opacity. The ratio of the off- to on-source fluxes at 1100 and 1300 μm in van der Veen et al. (1995) and Walmsley et al. (1991) may therefore partly reflect changes in the molecular line emission with radius rather than changes in the dust emission. The question of whether the mass loss rate has changed can not be answered without addressing these other issues as well and hence give a satisfactory account of the entire SED up to the cm wavelength region.

In Table 6 the constraints are compiled together with the different model results. Model A, the best fitting r^{-2} model, predicts about the correct fluxes up to $\sim$500 μm, too low on-source fluxes beyond $\sim$800 μm, too small flux-ratios and too small far-IR sizes. The latter fact conclusively shows that far from the star the dust density is underestimated in model A. This confirms earlier findings that the mass loss rate has been higher in the past.

To determine the change in the mass loss rate in an approximate way the following approach is adopted. First assume that $\dot{M}(t)$ is a step function: the mass loss rate is a factor f higher than the present-day value for dynamical ages greater than Δt

years. It is assumed that the expansion velocity, dust-to-gas ratio and dust opacity do not change with time. Calculations are presented with Δt = 1000, 3000, 4500 yr[2] (Models N, O, P). The respective values of $f = 4, 6, 9$ are determined to reasonably fit the observed size at 61 μm. The model with $\Delta t = 4500$ yr fits the 61 and 100 μm sizes simultaneously.

For comparison a model is calculated where the mass loss rate is continuously decreasing with time: $\dot{M}(t) = \dot{M}_0 \exp(-(t - t_0)/t_{1/2})$ where t_0 is an arbitrary starting time. $\dot{M}_0$ and $t_{1/2}$ are solved by imposing $\dot{M}_{present-day}$ at $t = t_{now}$ and a mass loss rate a factor f higher, Δt years ago (from which follows $t_{1/2} = \Delta t / \ln f$). Because of the exponential character the mass loss rate increases very fast with the dynamical age, and so does the total mass in the shell, which is given by $\Delta M = \dot{M}_0\, t_{1/2}\, (1 - \exp(t_0 - t_{now})/t_{1/2})$. In fact, the outer radius in the models was determined to give a total mass in the shell smaller than the maximum possible mass of about 7 M$_\odot$ (an initial mass of 8 M$_\odot$ minus a core mass of 1 M$_\odot$). The model that best fits the observed sized at 61 and 100 μm with this particular mass loss rate law is model Q with $t_{1/2}$= 6065 yr. The outer radius

---

[2] The dynamical ages are given for a distance of 135 pc and a dust velocity of 17.5 km s^{-1} and scale like D/v. In Table 4 the distance and velocity independent angular radii are listed.

Table 7. Model and observations in the cm-regime

Ref.[a]	λ	Flux	Aperture	Phase	Star[b]	Dust[c]	Star + free-free (mJy)[d]			Total flux (mJy)
	(cm)	(mJy)	($''$)		(mJy)	(mJy)	1600 K	2500 K	5000 K	Model R
1	0.33	145 ± 39	75	0.31	45.9	55.7 ± 7.0	46.3	46.3	46.3	150
2	1.5	4.1 ± 1.2	90	0.85	2.22	0.52 ± 0.17	2.52	2.49	2.47	4.25
	1.5	6.6 ± 0.4	90	0.30	2.22	0.52 ± 0.17	2.52	2.49	2.47	4.25
	2.0	1.40 ± 0.05	0.4	0.06	1.25	<0.004	1.55	1.53	1.50	1.54
3	2.0	1.16 ± 0.12	?	0.78	1.25	<0.01	1.55	1.53	1.50	1.56
	6.0	0.28 ± 0.05	?	0.78	0.14	<0.0004	0.40	0.40	0.40	0.40
4	3.6	0.77 ± 0.03	2.8	0.21	0.39	<0.003	0.68	0.67	0.64	0.69
5	6.0	0.42 ± 0.10	4.5	0.03	0.14	<0.0007	0.40	0.40	0.40	0.41

[a] References: 1 = Schwarz & Spencer (1977); 2 = Sahai et al. (1989); 3 = Drake et al. (1991); 4 = Knapp et al. (1995); 5 = Spergel et al. (1983).
[b] Flux of the stellar photosphere for T_{eff} = 2000 K. For the wavelength region of interest it is given by S_ν (Jy) = 2.00 $(2000/T_{eff})^3$ $(500\mu m/\lambda)^2$. This shows the largest uncertainty is the effective temperature. The uncertainty in the scaling factor is related to the error in L/D^2 which is known to within 5%. The angular diameter of the star is given by 70.2 $(2000/T_{eff})^2$ mas.
[c] Dust emission calculated for the parameters of model P extrapolated from the 400-1000 μm flux, taking into account beam effects. Error bars are 3σ values.
[d] Flux from the star and the free-free emission region for electron temperatures of 1600, 2500 and 5000 K, and other parameters as discussed in the text. The ionization fractions were fine tuned to give a 6 cm flux of 0.40 mJy.
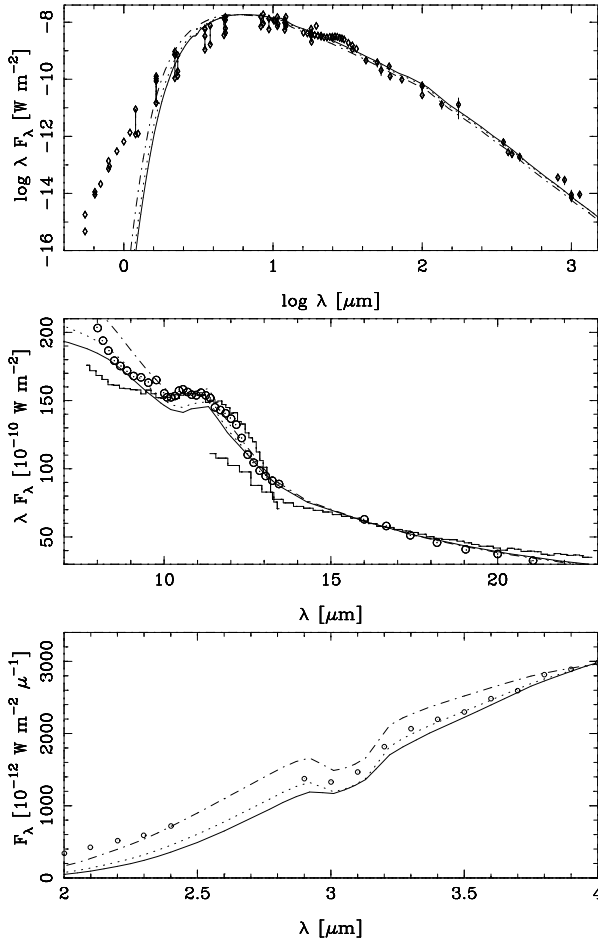
Fig. 9. Influence of velocity law. Models K (solid line; $\dot{M}$= 2.2 × 10^{-5} M$_\odot$ yr^{-1}), L (dash-dotted line; $\dot{M}$= 1.5 × 10^{-5} M$_\odot$ yr^{-1}) and M (dotted line; $\dot{M}$= 1.9 × 10^{-5} M$_\odot$ yr^{-1}, T_{eff} = 1800 K, T_c = 1000 K).

is located at ≈4300 condensation radii, corresponding to a dynamical age of ≈24000 yr. The mass loss rate at that epoch is 1.15×10^{-3} M$_\odot$/yr and the total mass in the shell is 6.85 M$_\odot$. Model Q fits the 61 and 100 μm sizes at the 2σ level and fits clearly less well than model P with the mass loss rate law in the shape of a step function. On the other hand it is not possible at the moment to claim that model P uniquely determines the dust density distribution. To further and better constrain the dust density distribution would require sensitive mapping at wavelengths $\gtrsim$100 μm out to as large as possible distances.

Sahai (1987) and Truong-Bach et al. (1991) present evidence for a higher mass loss rate in the past based on CO observations. Both find approximately a factor of 2 difference over a region of about 5$''$. It is not clear how to put this in the picture that emerges from the dust modeling. The far-IR sizes clearly imply variations over a much larger scale. On the other hand, small changes in the mass loss rate closer to the star may not give a clear signature in the dust emission.

3.3. Molecular lime emission

Model P fits the NIR sizes and the on-source fluxes up to ~400 μm well (with possibly a few exceptions) but fails to predict the observed fluxes for longer wavelengths.

It has been shown (Walmsley et al. 1991, Groesbeck et al. 1994) that molecular line emission can make a significant contribution to the broad-band fluxes. Main contributors are CO and HCN and their ^{13}C isotopes but numerous weaker lines as well. Groesbeck et al. (1994) estimate for IRC +10 216 a contribution of molecular line emission of 5.3 Jy in the 837-908 μm region (within the 18$''$ beam of the JCMT), and revised the estimate of 0.61 Jy by Walmsley et al (1991) up wards to 0.8 Jy for the 1300 μm passband (within the 11$''$ beam of IRAM). In Sect. 3.5 it is argued that molecular line emission may contribute even

up to 2.0 Jy in the IRAM beam near maximum light. On the other hand, beyond 3300 μm, the transition of HCN(1-0), there are no strong lines expected and the contribution of molecular line emission to broadband continuum observations should be small.

The difference in flux between model P and the observations at 900 μm of 6 Jy is consistent with the prediction of Groesbeck et al. This excellent agreement makes it at least plausible to ascribe the differences at 761 μm (2.9 Jy) and 811 μm (3.1 Jy) to the contribution of line emission as well. That the difference at these wavelengths is smaller is in part due to the fact that the strong ^{12}CO and ^{13}CO J=3-2 transitions are not located in these passbands.

In the 1000-1300 μm region the situation may be different. The difference at 1300 μm of 2.0 Jy between the model and the observations is larger than the 0.8 Jy contribution of line emission as estimated by Groesbeck et al. This leaves 1.2 Jy unaccounted for. The uncertainty in the flux of the stellar photosphere due to the uncertainty in $T_{\rm eff}$ is only 0.2 Jy (see later). This leaves two possibilities: a contribution of free-free emission, or a higher dust emissivity for $\lambda \gtrsim 1000$ μm. The latter assumption appears ad-hoc, but on the other hand no laboratory data is available at these wavelengths (the data in Rouleau & Martin 1991 go to 300 μm) and the opacities used so far have been calculated by extrapolating the optical constants.

To estimate the possible effect of free-free emission and the slope of the dust opacity beyond 1000 μm the observed fluxes in the cm region are studied in the next section.

3.4. Free-free emission

Since free-free emission increases approximately as λ^2 for large λ the cm-region is the suitable wavelength region to study the possible effect of free-free emission. The available observations for IRC +10 216 are listed in Table 7. The beam width used by Drake et al. (1991) is not given and is assumed in the calculations below to be 1″. Additionally, Drake et al. determined the size at 2 cm and found a FWHM of 80 x 59 mas (with a position angle of 41°), which may be translated into arithmetic and geometric means of 70 and 69 mas, respectively. The relevance of this observation is discussed in Groenewegen (1996).

When the contributions of free-free emission is considered one usually assumes the emission to be optically thick (e.g., Knapp et al. 1995). This assumption needs verification and may be valid only for a limited wavelength region as $\tau_{\rm free-free} \approx \lambda^2$. An additional complication is, when $\tau_{\rm free-free} \approx 1$, that it is not allowed to add the stellar flux and the free-free emission, as part of the stellar radiation is absorbed.

To circumvent all unnecessary assumptions full radiative transfer calculations are performed to calculate the flux of a central star and a region where free-free emission is assumed to occur. The details of the model are outlined in Appendix A. In short, the central star is surrounded by a spherical region out to radius $R_{\rm out}$ where free electrons are present. The H-density is calculated from the gas continuity equation (taking the mass loss rate from the dust models and $v_{\rm gas} = 14.5$ km s^{-1}). The electron

density is calculated by multiplying the hydrogen density with a constant 'ionization fraction'. The ion density is assumed equal to the electron density. The electron temperature is assumed to follow $T = T_0 (R_\star/r)^\gamma$. For the moment $R_{\rm out} = 4\,R_\star$ (the 'chromosphere' should always be smaller than the inner dust radius) and $\gamma = 0$ are assumed.

The calculations proceed as follows. For the parameters of model P the SED is calculated taking into account the apertures of the observations in Table 7. The stellar flux (Table 7, column 6) is subtracted to get the dust emission. The dust emission between 400 and 1000 μm is approximated as $\lambda^{-\epsilon}$ and used to estimate the dust emission at longer wavelengths (Table 7, column 7)[3]. Then the model in Appendix A is used to predict the flux of the central star and the free-free emission region (Table 7, columns 8-10) for $T_0 = 1600$, 2500 and 5000 K. In each case the ionization fraction is fine tuned in such a way that the total emission (star + dust + free-free) at 6 cm equals 0.40 mJy. The ionization fractions for the $T_0 = 1600$, 2500 and 5000 K models are 8.3×10^{-5}, 7.8×10^{-5} and 7.8×10^{-5} respectively. These ionization fractions are similar to those derived by Spergel (1983; $< 4 \times 10^{-5}$) and Drake et al. (1991; $< 10^{-4}$) using much simpler analyses. The derived ionization fraction depends on the assumed distance like $\sqrt{\rm distance}$.

Several things are obvious from these calculations: (A) In small apertures ($<5''$) dust emission is negligible, and (B) free-free emission is negligible at 3300 μm (and shorter) wavelengths. Furthermore the derived ionization fraction is almost independent of the assumed electron temperature. The calculated FWHM sizes at 2 cm are 70.2 mas for all three models. This is equal to the diameter of the star which means that the emission from the free-free region does not significantly broaden the 2 cm emission region. This implies that the free-free emission is optically thin at 2 cm which is confirmed by the calculations. The optical depths at 1.5, 2, 3.6 and 6 cm in the model with $T_0 = 2500$ K are 0.014, 0.026, 0.09 and 0.27, respectively. The free-free emission is about 0.27 mJy over most of the wavelength region consistent with the theoretical prediction that $S_\nu \sim \nu^{0.1}$ in the optically thin case.

The ionization fraction and T_0 are related since, according to the Saha-equation, $n_{\rm H^+}/n_{\rm H}$ is a function of T_0 (see Eq. 3-132 in Lang 1980). An ionization fraction of $\sim 8 \times 10^{-5}$ corresponds to a temperature of about 2400 K. This suggests that the free-free emission around IRC +10 216 is not due to a chromosphere but rather a (small) region with temperatures close to that of the photosphere where free electrons are present. The free-free model assumes a constant velocity in the free-free emission region. This likely underestimates the density close to the star and hence overestimates the ionization fraction. The typical electron temperature in the free-free emission region is therefore likely to be even lower than 2400 K.

The fact that free-free emission is negligible at 1300 and 3300 μm makes is at least plausible that the dust emission coef-

---

[3] The value of ϵ does not depend very strongly on the limits of 400 and 1000 μm and is found to be between 3.11 and 3.38. The errors quoted in Table 7, column 7 are based on an error of ± 0.1 in ϵ.
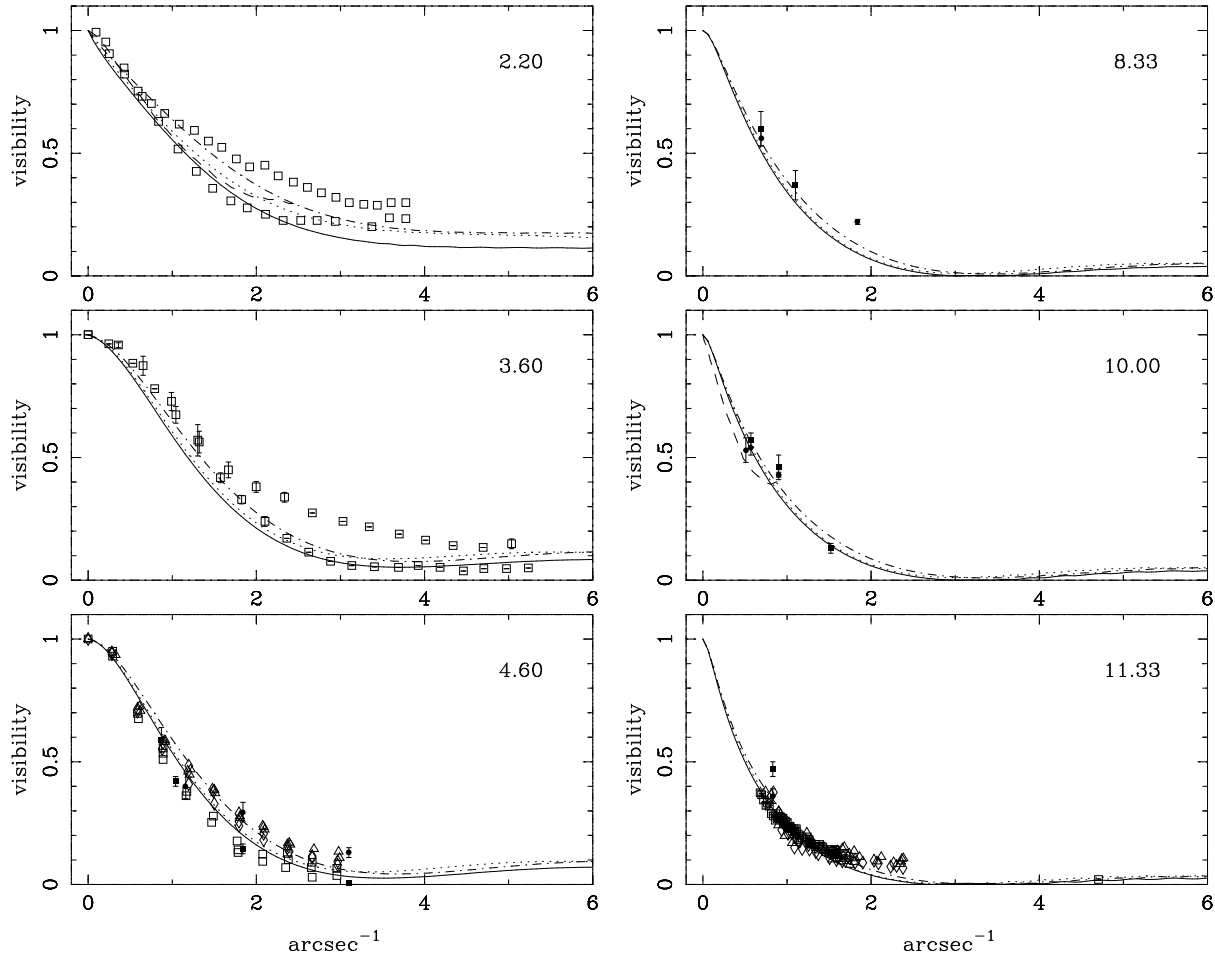
Fig. 10. Influence of velocity law. Models K (solid line; $\dot{M}$= 2.2 × 10^{-5} M$_\odot$ yr^{-1}), L (dash-dotted line; $\dot{M}$= 1.5 × 10^{-5} M$_\odot$ yr^{-1}) and M (dotted line; $\dot{M}$= 1.9 × 10^{-5} M$_\odot$ yr^{-1}, $T_{\rm eff}$ = 1800 K, $T_{\rm c}$ = 1000 K).

ficient beyond ∼ 1000 μm has been underestimated. The uncertainty in the stellar flux is small (also see discussion later), and the contribution of molecular line emission has already been discussed.

As a next step the dust emission coefficient is approximated as $Q_\lambda \sim \lambda^{-\alpha}$ for $\lambda \geq 1000$ μm and α is determined to fit the 3300 μm flux. I find $\alpha = 0.85$. The procedure is then similar to the earlier calculations: the dust emission is calculated and extrapolated to longer wavelengths and the ionization fraction is determined to fit the total 6 cm flux. This is done for $T_0 = 2500$ K. The ionization fraction is 7.8×10^{-5}. The result is model R (Table 6 and Table 7, column 11) which is the overall best fitting model. The optical depths are the same as for model P. The FWHM of the brightness distribution at 6 cm is predicted to be 91 mas. At 3.6 cm and shorter wavelengths it is 70 mas.

The calculations above have been performed for an effective temperature of the central star of 2000 K. From the fitting of the visibility curves the effective temperature was determined to be in the range 1700-2300 K. The cm observations put additional constraints on $T_{\rm eff}$. This is discussed in Groenewegen (1996),

and the outcome is that the cm observations limit the value of $T_{\rm eff}$ to 2000 ± 50 K.

3.5. Summary

The results of the non-r^{-2} models are briefly summarized here. It is found that a model which takes into account the fact that the dust velocity is a function of radius gives a slightly worse fit to the SED, the 2-4 and 8-24 μm spectra and visibility curves than the r^{-2} model. In fact, the best-fitting model which includes the dust velocity profile (Model M) has an effective temperature of 1800 K, which is incompatible with the limit of >1860 K derived from the cm flux and size at 2 cm near maximum light (see Groenewegen 1996).

It is argued that the fact that the dust-to-gas ratio and the dust velocity both increase with radius has only a small net effect on the dust density distribution and that deviations from a r^{-2} law may be small close to the star.

The observed far-IR sizes immediately indicate that far from the star a r^{-2} law underestimates the dust density distribution. A good fit is obtained with a mass loss rate law that increases by a factor 9 for radii >123''.

The contributions of dust and free-free emission can be disentangled at cm wavelengths. Dust emission is negligible beyond ~2 cm and free-free emission is negligible at wavelengths shorter than ~0.5 cm. The dust opacity beyond ~1000 μm needs to be modified to $\lambda^{-0.85}$ to account for the observed flux at 3300 μm. The largest discrepancy between the observations and the best-fitting model R is at 1300 μm. It is suggested that molecular line emission may contribute up to 2.0 Jy in a 11″ beam in the 1300 μm passband near maximum light, larger than suggested by Walmsley et al. (1991; 0.6 Jy) and Groesbeck et al. (1994; 0.8 Jy), and 1.0 Jy in the 1100 μm passband in a 18″ beam. The difference with the estimates by Walmsley et al. and Groesbeck et al. may indicate that molecular line emission is also a function of phase or that a large number of small lines are contributing that have not been accounted for. It is interesting to note that close to minimum light, at phase 0.43, Walmsley et al. find a flux of 1.47 Jy which is consistent with 0.6 Jy of stellar and dust emission and 0.8 Jy of molecular line emission.

The typical ionization fraction found in the free-free emission region is about 8×10^{-5} which, according to the Saha equation, corresponds to a temperature of about 2400 K.

4. Discussion

4.1. Evolutionary picture

If the luminosity of CW Leo averaged over the light curve is about 10000 L$_\odot$, as based on the $P - L$ relation in Groenewegen & Whitelock (1996), then using the core mass–luminosity relation in Vassiliadis & Wood (1994) one can derive a core mass of 0.68 M$_\odot$. As the growth of the core during the entire AGB lifetime is small (e.g. Groenewegen & de Jong 1993) the final mass at the end of the AGB should be about 0.68-0.70 M$_\odot$. Using the initial-final mass relation derived from the synthetic AGB evolution model of Groenewegen et al. (1995) one then derives an initial mass of 3.4 ± 0.2 M$_\odot$ where the uncertainty includes the uncertainty in the recipe for the mass loss on the AGB. If the mean luminosity would be 6700 or 15000 L$_\odot$ the initial mass would be about 3.0 or 4.0 M$_\odot$, respectively. From the same evolutionary models the C/O ratio at the end of the AGB phase is predicted to be 3.6, 3.6 and 3.1 for stars of initial mass 3.0, 3.4 and 4.0 M$_\odot$, respectively. The predicted maximum C/O ratio of 3.9 (in a model for an initial mass of 3.1 M$_\odot$) is in good agreement with the highest observed value in disk planetary nebulae. An initial mass between 3 and 5 M$_\odot$ was recently derived by Guélin et al. (1995) based on the observed isotopomers ^{25}MgNC and ^{26}MgNC and evolutionary model calculations.

An arbitrary dust-to-gas ratio of 0.005 was assumed in the models to convert the dust mass loss rate into a gas mass loss rate. There is a physical upper limit to the dust-to-gas ratio based on the number of atoms that can condense into dust. Using the continuity equation for the gas and the dust and assuming that the dust is 100% carbonaceous one may derive that the theoretical dust-to-gas ratio is given by:

$$\Psi = f_c \, (C/O - 1) \frac{n_O}{n_H} \frac{12}{1.4} \frac{v_{gas} + v_{dr}}{v_{gas}} \tag{8}$$

where f_c is the degree of condensation and C/O the number ratio of carbon to oxygen atoms. Assuming a constant gas velocity of 14.5 km s^{-1} and a drift velocity of 3.0 km s^{-1} and a cosmic oxygen abundance of 8.70 (on a scale where H = 12.0) then the theoretically predicted dust-to-gas ratio is $\Psi = f_c$ (C/O -1) 5.18×10^{-3}.

As C/O < 4 and $f_c < 1$ it follows that $\Psi < 0.016$. This upper limit is valid for all carbon stars. Calculations show that f_c is about 0.4 (within a factor of 2) (see Fleischer et al. 1995, Winters et al. 1994) and for CW Leo a C/O estimate of 2-3 seems appropriate. In that case Ψ should be in the range 0.001 - 0.008. The default dust-to-gas ratio used in the model calculations of 0.005 agrees with the theoretical range.

4.2. Scattering and grain size distribution

The calculations have been performed with the AC species of amorphous carbon in Rouleau & Martin (1991). To check the influence of that assumption calculations were performed with the other species listed by them, designated BE1, FC21 and HAPS, and for the optical constants listed in Hanner (1988). I recall that AC stands for soot produced by striking an arc between two amorphous carbon electrodes, BE is soot produced from benzene burned in air, while FC21 (fractal clustering) and HAPS (homogeneous aggregates) are variants of BE used to illustrate the effect of clustering on the optical constants. BE, FC21 and HAPS grains give almost identical best fitting grain sizes of 0.15 μm, essentially the same as for AC grains. The optical sizes are best fitted with AC grains. For the optical constants of Hanner (1988) a best fitting grain size of 0.14 μm is found. The main difference of the BE and Hanner grains is that due to the difference in the absolute opacity the best fitting dust mass loss rate is about a factor of two lower than for AC grains.

In the models a single grain size is assumed. Many authors have used a grain size distribution (Griffin 1990, Danchi 1994, Jura 1994, B95, IE96). In all cases the authors assume a size distribution similar to the one observed in the ISM without apparent justification (i.e., $n(a) \sim a^{-3.5} \exp(-a/a_0)$ with $a_{min} < a < a_{max}$). However, detailed modeling of the formation and growth of dust particles around (carbon-rich) AGB stars (Dominik et al. 1989, 1993; Höfner & Dorfi 1992) suggest that the particle size distribution has a maximum at some grain size with tails to both smaller and larger grains. To constrain the presence of smaller and larger grains models are calculated for $a = 0.05$ and 0.5 μm. Surface brightnesses $I(p) = y \times I(p, a = 0.16 \mu m) + (1 - y) \times I(p, a = 0.05 \mu m$ [or $0.5 \mu m$]) are constructed from which the SED, the visibility curves and the optical FWHM sizes are calculated. The value of y is then determined in such a way to make the models just consistent with the observations. For $a = 0.05$ μm I find $y > 0.85$, and for $a = 0.5$ μm, $y > 0.90$. This suggests that the initial assumption of a dominant grain size is reasonable. There are no combinations of models with 0.05 and 0.5 μm grains thats fit the visibility curves.

Jura (1994) recently argues for the presence of grains as small as 0.015 μm. Interstellar UV light penetrates the circum-

stellar shell (depending on the optical depth in the UV) and dissociates some types of molecules. Some of these daughter species are observed to display ring-like structures at about 15″ from the central star (see references in Jura 1994). From a qualitative calculation he then estimates from the condition $\tau_{0.1\mu m}$ = 2 from r = 15″ to infinity that grains of 0.015 μm should exist. For model A I find $\tau_{0.1\mu m}$ = 56 from r_c to r_{outer} which translates into $\tau_{0.1\mu m}$ = 0.58 from r = 15″ to r_{outer}. Model D, with a = 0.05 μm grains, gives $\tau_{0.1\mu m}$ = 2.1 from r = 15″ to r_{outer}. This possibly indicates a need for some smaller grains, but the calculations suggest rather a size of 0.05 μm than 0.015 μm. The calculations in the previous paragraph indicate that a contribution of grains of size 0.05 μm of up to 15% is consistent with the data. This result is independent of the assumed distance to the source since the angular sizes in the envelope scale with the stellar radius and distance like $R_\star/D \sim \sqrt{L/D^2}/T_{eff}^2$, which is independent of distance, as L/d^2 is the total observed flux at earth.

The modeling in this paper suggests that grains of radius 0.16 μm fit the visibility curves and the optical sizes best. This result appears to be independent of the exact choice of the optical constants. Previously, Daniel (1982) modeled IRC +10 216 (and other stars) in terms of a bipolar nebula and found that good agreement with polarization data could be achieved with grains of size 0.1 and 0.35 μm, with a ratio in optical depth of about 90. In a recent paper Ivezić & Elitzur also put forward arguments in favor of the presence of large grains in CW Leo. In another quantitative study, Seab & Snow (1989) showed from UV extinction curves that grains of size $\lesssim$0.08 μm can not exist in the shell around the supergiant α Ori. This is another indication that the usual assumption of small grains in the shells around late-type stars may not necessarily be justified.

The method presented here to model the NIR visibility curves to estimate the grain size is a powerful method that can be applied to other AGB stars as well. Determining the grain size in more AGB stars should provide valuable constraints on the grain formation and growth process and allow a comparison with grains (sizes) in the interstellar medium.

The calculations in Sect. 3.1 indicate that models with large grain sizes fit the visibility curves and optical sizes quite well but result in a significant deficiency in the flux at optical wavelengths. An alternative model is one with small grains which fits the SED but not the optical sizes and visibility curves. The former model is preferred and the deficiency in the optical flux is interpreted as related to the asymmetry of the shell. An additional uncertainty might be the properties of the dust grains (uncertain asymmetry factor, non-spherical grains that may or may not be randomly oriented, grain growth which implies smaller grains closer to the star). Recently, Sloan & Egan (1995) discussed the existence of a region of "blue emission" about 1″ north of the star. They suggest that the inner part of the shell can be described by a nearly spherical shell with evacuated poles.

4.3. The inner dust temperature

The results of the modeling indicate that T_c = 1075 $\pm$ 50 K in good agreement with earlier work (Martin & Rogers 1987, Ridgway & Keady 1988) and contrary to the result of Danchi et al. (1994). The most likely explanation for this discrepancy is that the visibility curve and flux at 11 μm sample dust of about 250 K and therefore are not very sensitive to the hot dust (> 1000 K) at the inner radius which is best studied at 2-3 μm.

4.4. The density law

By artificially decreasing the outer radius it is found that the presently available constraints are not sensitive to the dust density beyond $\sim$10′ (corresponding to a dynamical age of about 22 000 yr at a distance of 135 pc). For example, decreasing R_{outer} from 7100 to 4000 r_c (= 10′) decreases the FWHM size at 61 μm from only 52.5″ to 51.2″ and the FWHM size at 100 μm from 282″ to 264″. The total dust mass in the shell out to 10′ is 1.0 $(D$ (kpc)$)^2$ M$_\odot$ in model R.

The fact that the far-IR fluxes are larger than predicted for the constant mass loss rate model could also in part be due to an interaction of the outer parts of the wind with the ISM. Depending on the density of the ISM, the circumstellar wind will slow down leading to an enhancement of the density and dust emission compared to a r^{-2} distribution (see e.g. Le Sidaner & Le Bertre 1993). To simulate this effect the dust density due to the circumstellar shell is artificially enhanced at every radial grid point in the model by the interstellar dust density calculated from a H-density of 2 cm^{-3} and a dust-to-gas ratio of 0.01. The H-density corresponds to the density in the Galactic plane (Spitzer 1978) and therefore is an upper limit to the density at the height above the plane where IRC +10216 is located. The calculations show that this effect is negligible. The reason is that the effects occur far out in the shell which are not traced by any of the observational constraints. The simplifying assumption that the grain properties (optical constants, density and grain size) for the interstellar dust are identical to those of the circumstellar dust do not change that conclusion.

Appendix A: free-free emission

In this appendix the treatment of free-free emission is described taking into account the emission of the central star and optical depth effects. The geometry of the problem is sketched in Fig. 11. A central star of effective temperature T_{eff} and radius $R_\star$ is surrounded by a spherical shell of radius R_{out}. Free electrons are present in this region, but it is assumed there is no
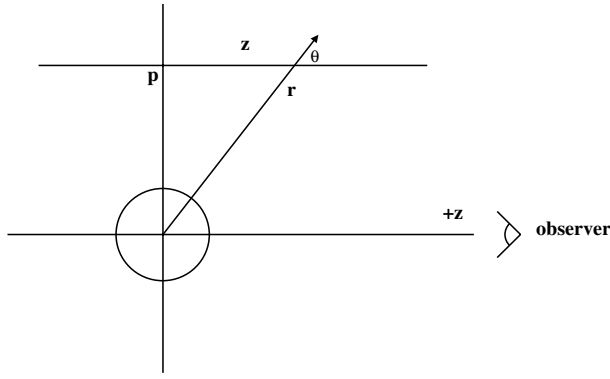
Fig. 11. The geometry of the problem with a central star, the impact parameter (p), radial distance (r) and $z = \sqrt{r^2 - p^2}$.

dust. This latter assumption is valid since R_{out} (identified with the extent of the 'chromosphere') can reasonably be assumed to be smaller than the inner dust radius.

For each impact parameter, p, the radiative transfer equation is solved along the z-axis for the specific intensity I for a given wavelength

$$I_\lambda(p) = I_0 \, e^{-\int_{z_0}^{z_{\text{m}}} \alpha(r')dz'}$$
$$+ \int_{z_0}^{z_{\text{m}}} \alpha(r') \, B_\lambda(T(r')) \, e^{-\int_{z'}^{z_{\text{m}}} \alpha(r'')dz''} \, dz' \quad \text{(A1)}$$

where $z_{\text{m}} = +\sqrt{R_{\text{out}}^2 - p^2}$, $B_\lambda(T(r))$ the Planck function with the electron temperature and α the absorption coefficient. The quantities I_0 and z_0 are 0 and $-\sqrt{R_{\text{out}}^2 - p^2}$ when $p > R_\star$ and $B_\lambda(T_{\text{eff}})$ and $+\sqrt{R_\star^2 - p^2}$ when $p \leq R_\star$. Dust extinction in the wavelength region of interest in entirely negligible, so the intensity at $z = z_{\text{m}}$ equals the intensity at $z = +\infty$ (the observer).

The absorption coefficient (in cm^{-1}) is given by

$$\alpha = 1.3703 \times 10^{-35} \, g \, \lambda^3 \, Z^2 \, n_e \, n_i$$
$$\star \, (1 - \exp(-14387.7/\lambda/T))/T^{0.5} \quad \text{(A2)}$$

where λ is the wavelength in micron, g the Gaunt factor, Z the charge of the ions (assumed 1), T the electron temperature and n_e and n_i the electron and ion density. The H-density is calculated from an assumed mass loss rate and gas expansion velocity and follows an r^{-2} law. The ion density is calculated from the H-density by multiplying by a constant 'ionisation fraction'. The electron density is assumed to equal the ion density. The electron temperature is assumed to follow $T_0 \, (R_\star/r)^\gamma$. These assumptions are untested in the sense that the density and temperature structure close to the star are not known. The Gaunt factor has been calculated according to subroutines kindly provided by Dr. Alex de Koter (Goddard Space Flight Center, USA).

The flux at earth is calculated from

$$F_\lambda = \frac{2\pi}{D^2} \int_0^{R_{\text{out}}} I_\lambda(p) \, p \, dp \quad \text{(A3)}$$

where D is the distance to earth. The model also calculates the FWHM values of the surface brightness distribution $I_\lambda(p)$, and the flux distribution $p \, I_\lambda(p)$. Model parameters are R_{out}, the ionisation fraction and electron temperature (T_0 and γ). Other parameters that are constrained from the dust modeling are the mass loss rate and gas velocity to calculate the H-density, the effective temperature and radius of, and the distance to, the star.

The integrals in Eqs. (A1, A3) are solved using the trapezium rule. Tests show that for reasonable values for R_{out} (a few $R_\star$) 100 equidistant values for p and a similar number of points along the z-axis (except in extremely optically thick cases) give very accurate results.

References

Althenoff W.J., Thum C., Wendker H.J., 1994, A&A 281, 161

Ambramowitz M., Stegun I.A., 1972, Handbook of mathematical functions, Dover publications, New York

Bagnulo S., Doyle J.G., Griffin I.P., 1995, A&A 301, 501 (B95)

Becklin E.E., Frogel J.A., Hyland J.A., Kristian J., Neugebauer G., 1969, ApJ 158, L133

Bohren C.F., Huffman D.R., 1983, Absorpion and scattering of light by small particles, John Wiley & Sons, New York (Appendix A)

Bracewell R.N., 1986, The Fourier transform and its application, McGraw-Hill

Cambell M.F., et al., 1976, ApJ 208, 396

Cardelli J.A., Clayton G.C., Mathis J.S., 1989, ApJ 345, 245

Cohen M., Walker R.G., Witteborn F.C., 1992, AJ 104, 2030

Daniel J.-Y., 1982, A&A 111, 58

Danchi W.C., Bester M., Degiacomi C.G., Greenhill L.J., Townes C.H., 1994, AJ 107, 1469

Dominik C., Gail H.-P., Sedlmayer E., 1989, A&A 223, 227

Dominik C., Sedlmayer E., Gail H.-P., 1993, A&A 277, 578

Drake S.A., Linksky J.L., Judge P.G., Elitzur M., 1991, AJ 101, 230

Dyck H.M., Zuckerman B., Leinert Ch., Beckwith S., 1984, ApJ 287, 801

Dyck H.M., Zuckerman B., Howell R.R., Beckwith S., 1987, PASP 99, 99

Elias J.H., et al., 1978, ApJ 220, 25

Fazio G.G., McBreen B., Stier M.T., Wright E.L., 1980, ApJ 237, L39

Fleischer A.J., Gauger A., Sedlmayr E., 1995, A&A 297, 543

Griffin I.P., 1990, MNRAS 247, 591

Groenewegen M.A.T., 1993, Chapter 5, Ph.D. thesis, University of Amsterdam

Groenewegen M.A.T., de Jong T., 1993, A&A 267, 410

Groenewegen M.A.T., de Jong T., Geballe T.R., 1994, A&A 287, 163

Groenewegen M.A.T., 1995, A&A 293, 463

Groenewegen M.A.T., Van den Hoek L.B., de Jong T., 1995, A&A 293, 381

Groenewegen M.A.T., 1996, A&A 305, L61

Groenewegen M.A.T., Whitelock P.A., 1996, MNRAS, in press

Groesbeck T.D., Phillips T.G., Blake G.A., 1994, ApJS 94, 147

Guélin M., Forestini M., Valiron P., Ziurys L.M., Anderson M.A., Cernicharo J., Kahane C., 1995, A&A 297, 183

Habing H.J., Tignon J., Tielens A.G.G.M., 1994, A&A 286, 523

Hackwell J.A., 1972, A&A 21, 239

Hanner M.S., 1988, Infrared observations of comets Halley and Wilson and properties of the grains, NASA CP3004, p. 22

Harvey P.M., Lester D.F., Brock D., Joy M., 1991, ApJ 368, 558

Herter T., Briotta Jr. D.A., Gull G.E., Houck J.R., 1982, ApJ 259, L25

Höfner S., Dorfi E.A., 1992, A&A 265, 207

Ivezić Z., Elitzur M., 1996, MNRAS 279, 1011 (IE96)

Joint IRAS Science Working Group, 1986, IRAS catalogs and atlases, Low Resolution Spectrograph (LRS), A&AS 65, 607

Joint IRAS Science Working Group, 1986, IRAS catalogs and atlases, Point Source Catalog (PSC), US Government Printing Office, Washington

Joint IRAS Science Working Group, 1986, IRAS catalogs and atlases, Explanatory Supplement, US Government Printing Office, Washington

Jones T.J., et al., 1990, ApJS 74, 785

Jura M., 1994, ApJ 434, 713 (J94)

Kastner J.H., Weintraub D.A., 1994, ApJ 434, 719

Keady J.J., Ridgway S.T., 1993, ApJ 406, 199

Knapp G.R., Bowers P.F., Young K., Phillips T.G., 1995, ApJ 429, L33

Lang K.R., 1980, in: Astrophysical Formulae, 2nd edition, Springer Verlag, p. 245

Le Bertre T., 1987, A&A 176, 107

Le Bertre T., 1988, A&A 203, 85

Le Bertre T., 1992, A&AS 94, 377

Le Sidaner P., Le Bertre T., 1993, A&A 278, 167

Lorenz-Martins S., Lefèvre J., 1993, A&A 280, 567

Low F.J., Rieke G.H., Armstrong K.R., 1973, ApJ 183, L105

Mariotti J.M., et al., 1983, A&A 120, 237

Martin P.G., Rogers C., 1987, ApJ 322, 374

Marshall C.R., Leahy D.A., Kwok S., 1992, PASP, 104, 397

McCarthy D.W., Howell R., Low F.J., 1980, ApJ 235, L27

Merrill K.M., Stein W., 1976, PASP 88, 294

Miller J.S., 1970, ApJ 161, L95

Mitchell R.M., Robinson G., 1980, MNRAS 190, 669

Netzer N., Elitzur M., 1993, ApJ 410, 701

Orofino V., Colangeli L., Bussoletti E., Blanco A., Fonti S., 1990, A&A 231, 105

Pégourié B., 1988, A&A 194, 335

Phillips J.P., et al., 1982, A&A 116, 130

Rengarajan T.N., et al., 1985, ApJ 289, 630

Ridgway S.T., Keady J.J., 1988, ApJ 326, 843

Rogers C., Martin P.G., 1984, ApJ 284, 327

Rowan-Robinson M., Harris S., 1983, MNRAS 202, 797

Rouleau F., Martin P.G., 1991, ApJ 377, 526

Sahai R., 1987, ApJ 318, 809

Sahai R., Claussen M.J., Masson C.R., 1989, A&A 220, 92

Schwarz P.R., Spencer J.H., 1977, MNRAS 180, 297

Seab C.G., Snow T.P., 1989, ApJ 347, 479

Sloan G.C., Egan M., 1995, ApJ 444, 452

Sopka R.J., et al., 1985, ApJ 294, 242

Spergel D.N., Giuliani J.L, Knapp G.R., 1983, ApJ 275, 330

Spitzer L., 1978, Physical processes in the interstellar medium, Wiley & Sons

Sutton E.C., Betz A.L., Storey J.W.V., Spears D.L., 1979, ApJ 230, L105

Treffers R., Cohen M., 1974, ApJ 188, 545

Truong-Bach, Morris D., Nguyen-Q-Rieu, 1991, A&A 249, 435

van der Veen W.E.C.J., Omont A., Habing H.J., Matthews H.E., 1995, A&A 295, 445

Vassiliadis, Wood P.R., 1994, ApJS 92, 125

Walmsley C.M., et al., 1991, A&A 248, 555

Winters J.M., 1994, Ph.D. thesis, Technische Universität Berlin

Winters J.M., Dominik C., Sedlmayer E., 1994, A&A 288, 255

Winters J.M., Fleischer A.J., Gauger A., Sedlmayer E., 1994, A&A 290, 623

Young K., Phillips T.G., Knapp G.R., 1993, ApJS 86, 517